Chapter – 4

Si-B-C-N Ceramics Derived from T2-1 Precursor

For the preparation of T2-1 derived material see Section 2.2. The as-thermolyzed materials investigated were annealed for crystallization according to the information provided in Table 4.1.

4.1 Results

4.1.1 Chemical analyses

Chemical analyses were carried out for all the crystallized samples. Table 4.1 gives the weight percentage of the elements in the samples analyzed. The materials given in the table were prepared using polymer particles in the size range 80 μm – 160 μm, except for ones the indicated by an asterisk (*) which were prepared using 32 μm – 80 μm particles to study the influence of the size of the polymer particles. The first two rows are highlighted because these materials were subsequently investigated for their high temperature deformation behavior.

Crystallized Material	Si % Wt.	B % Wt.	C % Wt.	N % Wt.	H % Wt.	O % Wt.
Methods of Detection	XRF	ICP - OES	Vario EL	TC-436 & Vario EL	Vario EL	TC-436
1800 °C, 3 h-1 MPa N_2	43.8	6.15	32.10	16.9	< 0.1	1.3
1900 °C, 3 h-1 MPa N_2	46.4	5.80	32.00	15.2	< 0.1	0.2
1900 °C, * 3 h-1 MPa N_2	48.9	6.96	33.10	10.7	< 0.1	0.9
1800 °C, 10 h-1 MPa N_2	43.0	5.90	32.30	15.9	< 0.1	2.9
1800 °C, * 10 h-1 MPa N_2	47.1	6.30	32.50	13.0	< 0.1	1.0

Table: 4.1 Chemical analyses for all the crystallized samples using various analytical techniques (* polymer particle size 32 μm – 80 μm).

4.1.2 Weight loss and density increase after crystallization

As observed in the histograms (Figure 4.1) there is a weight loss of around 3 % for materials produced using polymer particles in the size range of 80 μm – 160 μm, annealed at 1800 °C for about 3 h. If the heat treatment temperature is increased by 100 °C at the same holding time a weight loss of around 5.5 % is recorded. For the same heat treatment conditions (1900 °C , 3 h), the material produced using the smaller size fraction of polymer particles (32 μm – 80 μm) experiences a weight loss of around 11 % demonstrating a distinct influence of the size of the polymer particles on the decomposition/degassing behavior.

When the holding time is increased from 3 h to 10 h, materials annealed at 1800 °C show a weight loss of around 4.3 %. When this material is produced using polymer particles in the size range 32 μm – 80 μm, a weight loss of around 8.5 % is recorded. It is clearly observed that the weight loss is always doubled when the smaller size fraction of the polymer particles is used for processing. This effect is understandable due to the larger surface area to volume ratio of the particles as the size of the particles is reduced. The increase in density during post-annealing treatments is also shown in Figure 4.1. For all samples, values between 6 % - 8.8 % were measured for the weight loss, with the maximum increase occurring for the material annealed at 1800 °C for 3 h. Increasing the temperature or holding time does not result in an appreciable increase in density.

4.1.3 Structural Characterization: XRD, TEM, EFTEM

Structural characterization of T2-1 derived nano-crystalline Si-B-C-N ceramics obtained after annealing at the two different temperatures 1800 °C and 1900 °C and for the two different holding times 3 h and 10 h was carried out to investigate the influence of these processing parameters on the crystallization behavior. The influence of the size of the initial polymer particles was also investigated.

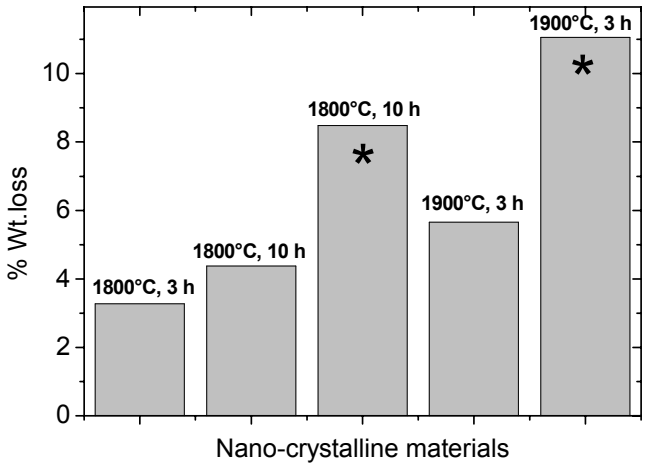

(a)

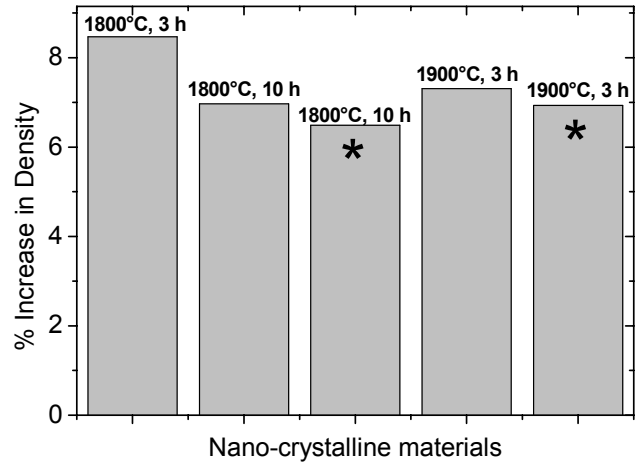

(b)

Figure: 4.1 Weight loss and increase in density of nano-crystalline Si-B-C-N ceramics after annealing for 3 h and 10 h at temperatures of 1800 °C and 1900 °C. All the materials were held at a constant overpressure of nitrogen of 1 MPa.

X – ray diffraction patterns were recorded for the crystallized samples as shown in Figure 4.2 (a to e). The insets in these diagrams are bright field TEM micrographs of the respective microstructures which indicate the morphology and distribution of the crystallites as reflected in the X - ray patterns. The Bragg reflections correspond to SiC and Si_3N_4. The intensity of

the silicon nitride peaks is reduced with decreasing size of the polymer particles as a result of decomposition reactions.

An analogous observation is made by energy filtering transmission electron microscopy (EFTEM). By using EFTEM qualitative and quantitative information about the elemental distribution can be gathered. In the present case, electron spectroscopic images (ESI) were recorded which provide a qualitative analysis only. In the elemental maps shown in Figure 4.3, the bright areas and dark areas show the presence and absence of a particular element. In most cases, grains appear dark and the surrounding matrix phase appears lighter in the bright field images also included in Figure 4.3, and it is just vice versa in the low loss images. With the help of the elemental maps of Si, B, C and N, it is possible to identify the crystallites of SiC and Si_3N_4 unambiguously.

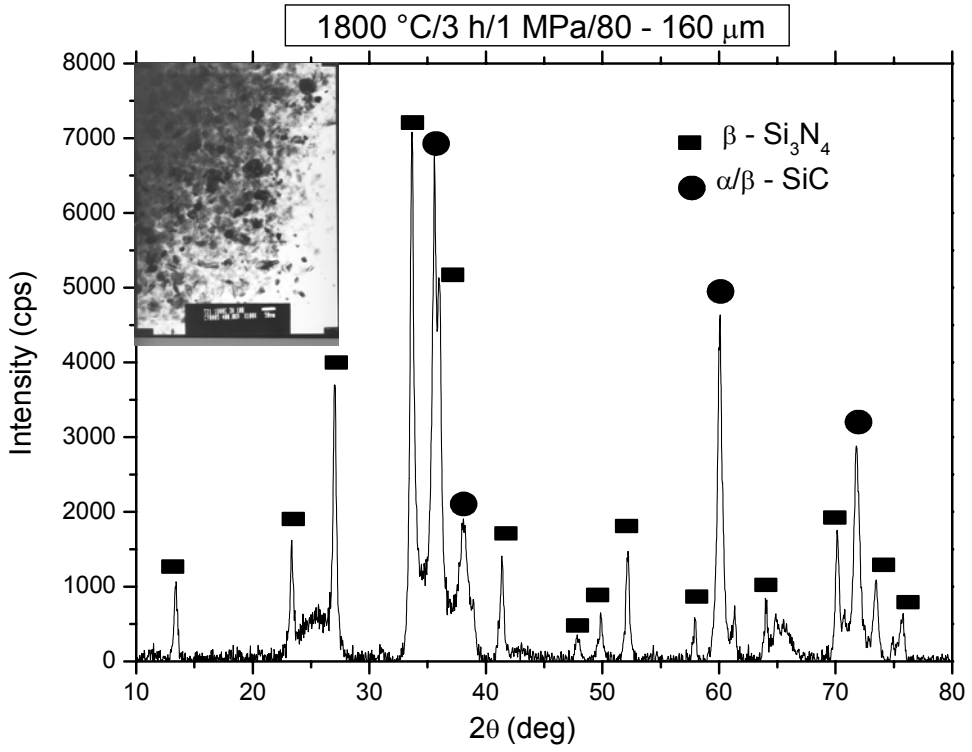

(a)

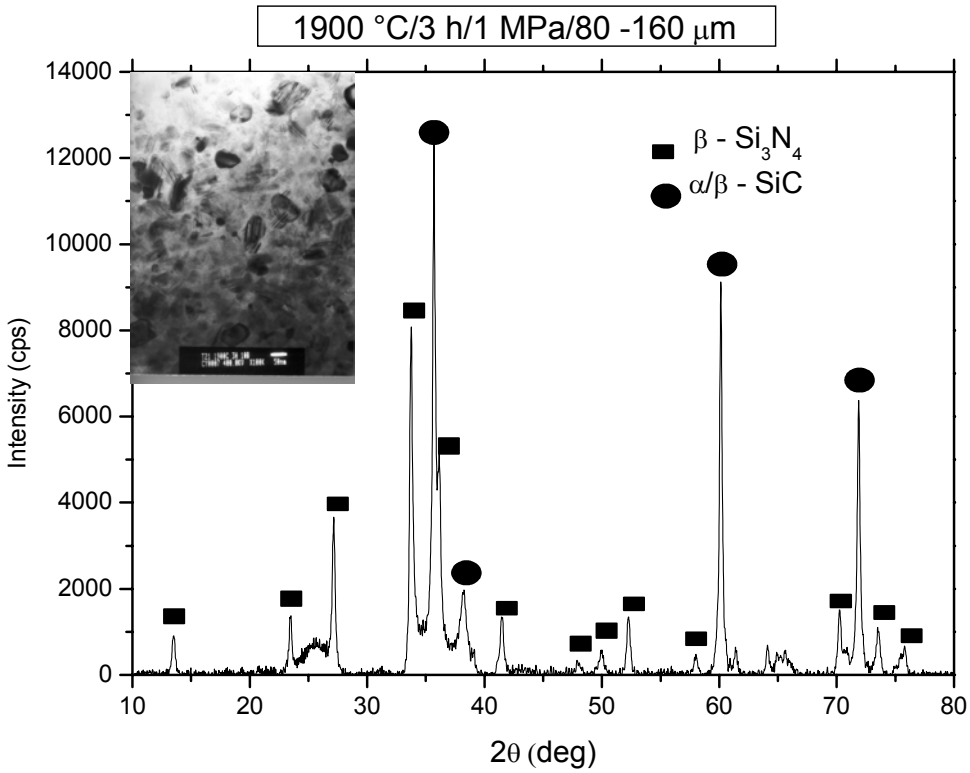
1900 °C/3 h/1 MPa/80 -160 μm
β - Si3N4
α/β - SiC
Intensity (cps)
2θ (deg)

(b)

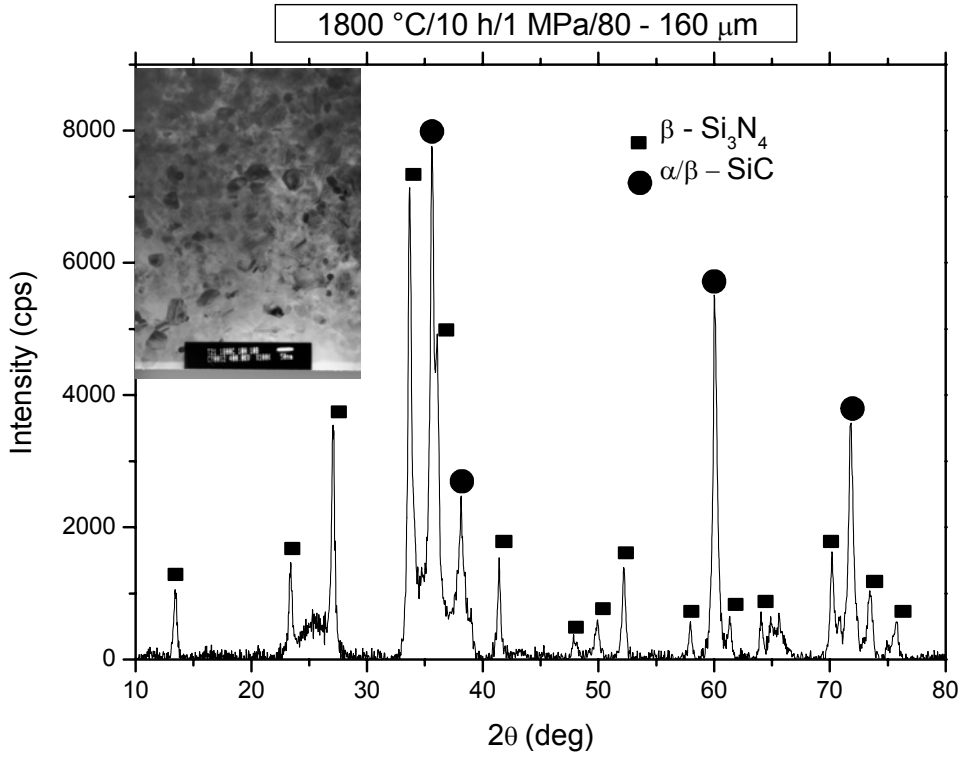
1800 °C/10 h/1 MPa/80 - 160 μm
β - Si3N4
α/β – SiC
Intensity (cps)
2θ (deg)

(c)

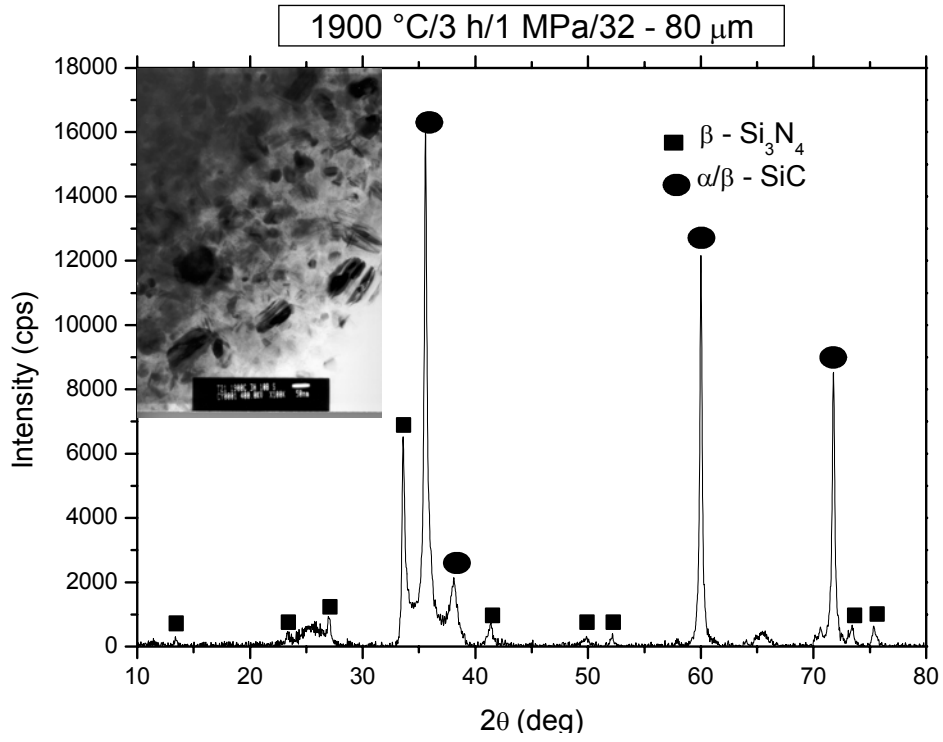

(d)

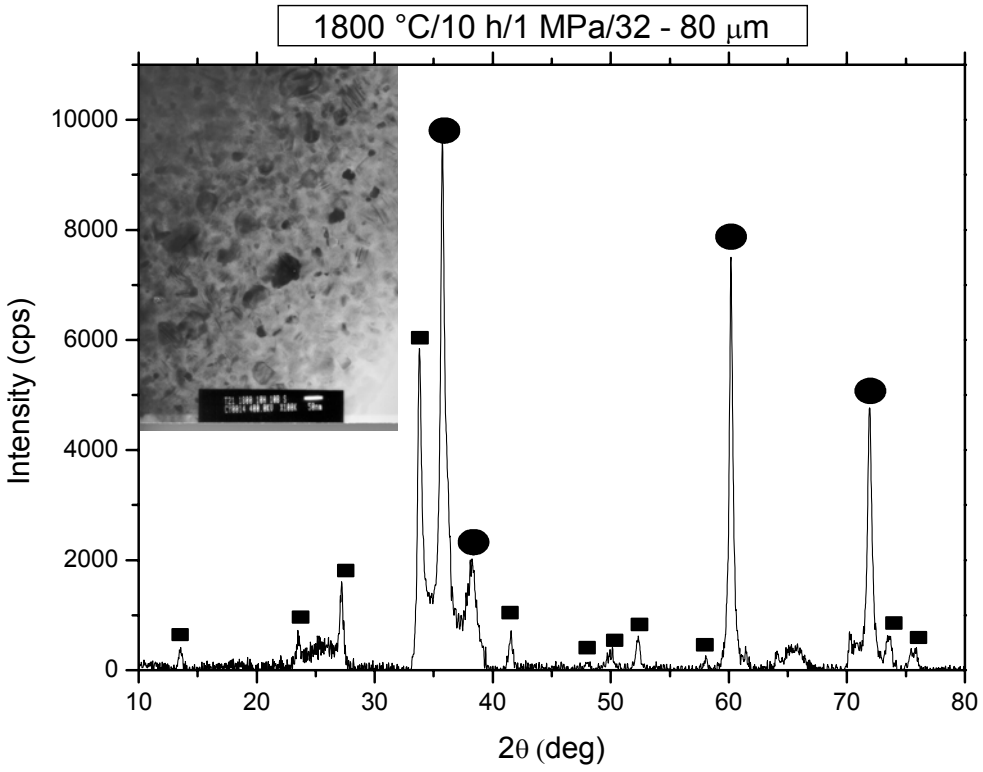

(e)

Figure: 4.2 XRD patterns along with TEM pictures of various crystallized Si-B-C-N ceramics showing the influence of annealing temperature, holding time and polymer particles size.

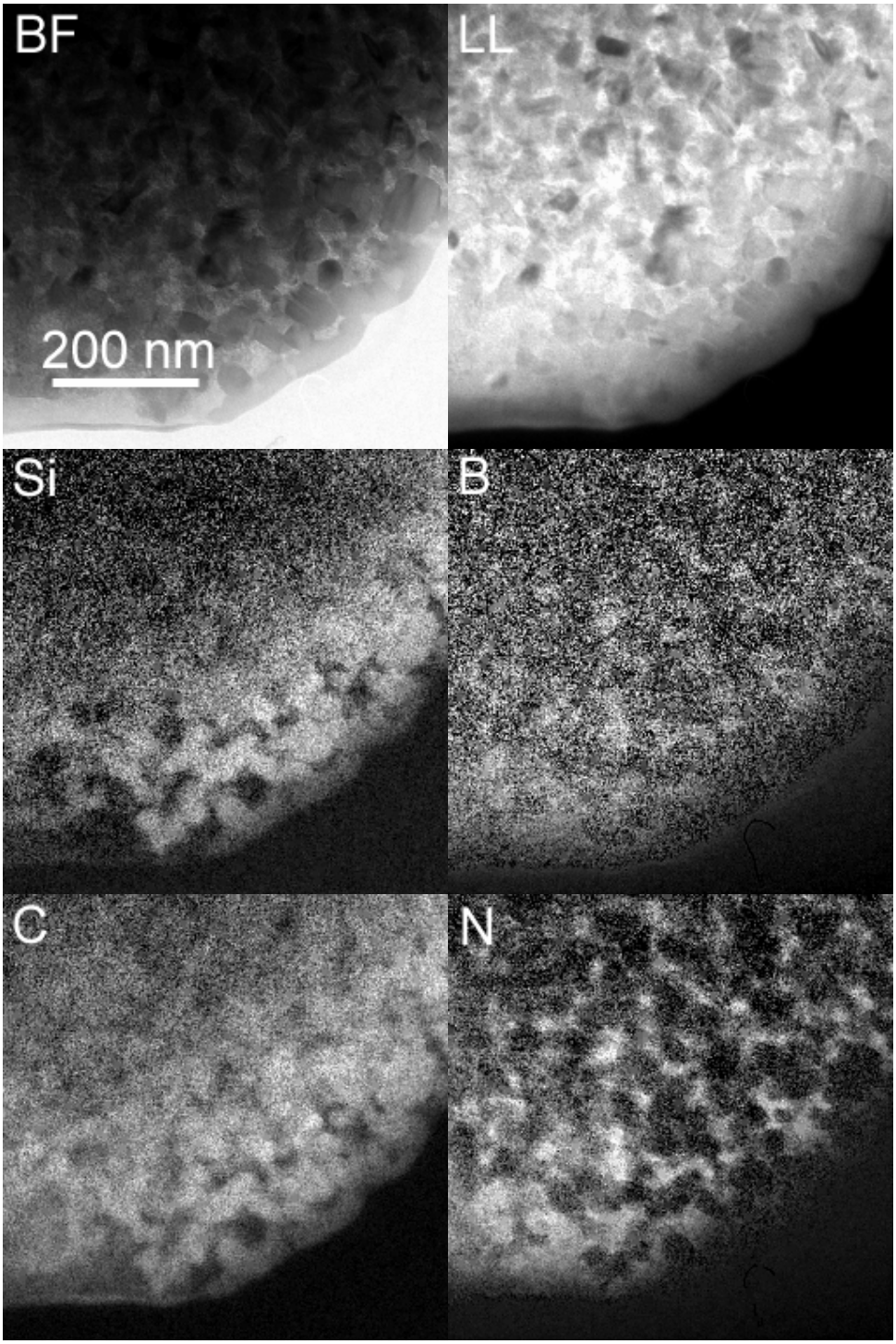

Figure: 4.3 (a) Bright field, low loss and elemental distribution images of Si-B-C-N ceramics crystallized at 1800 °C/3 h/1 MPa N_2 (80 - 160 μm).

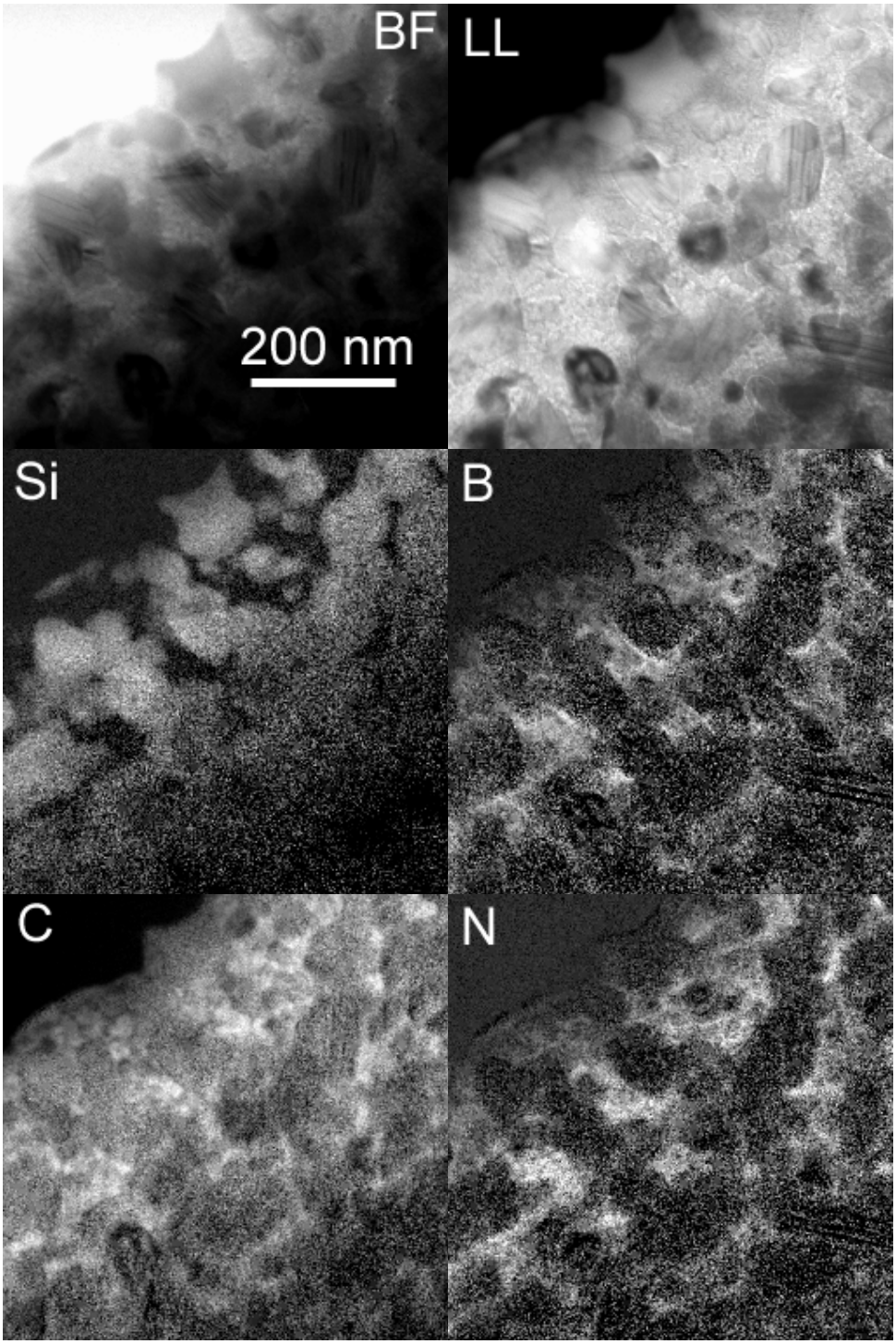

Figure: 4.3 (b) Bright field, low loss and elemental distribution images of Si-B-C-N ceramics crystallized at 1900 °C/3 h/1 MPa N_2 (80 - 160 μm).

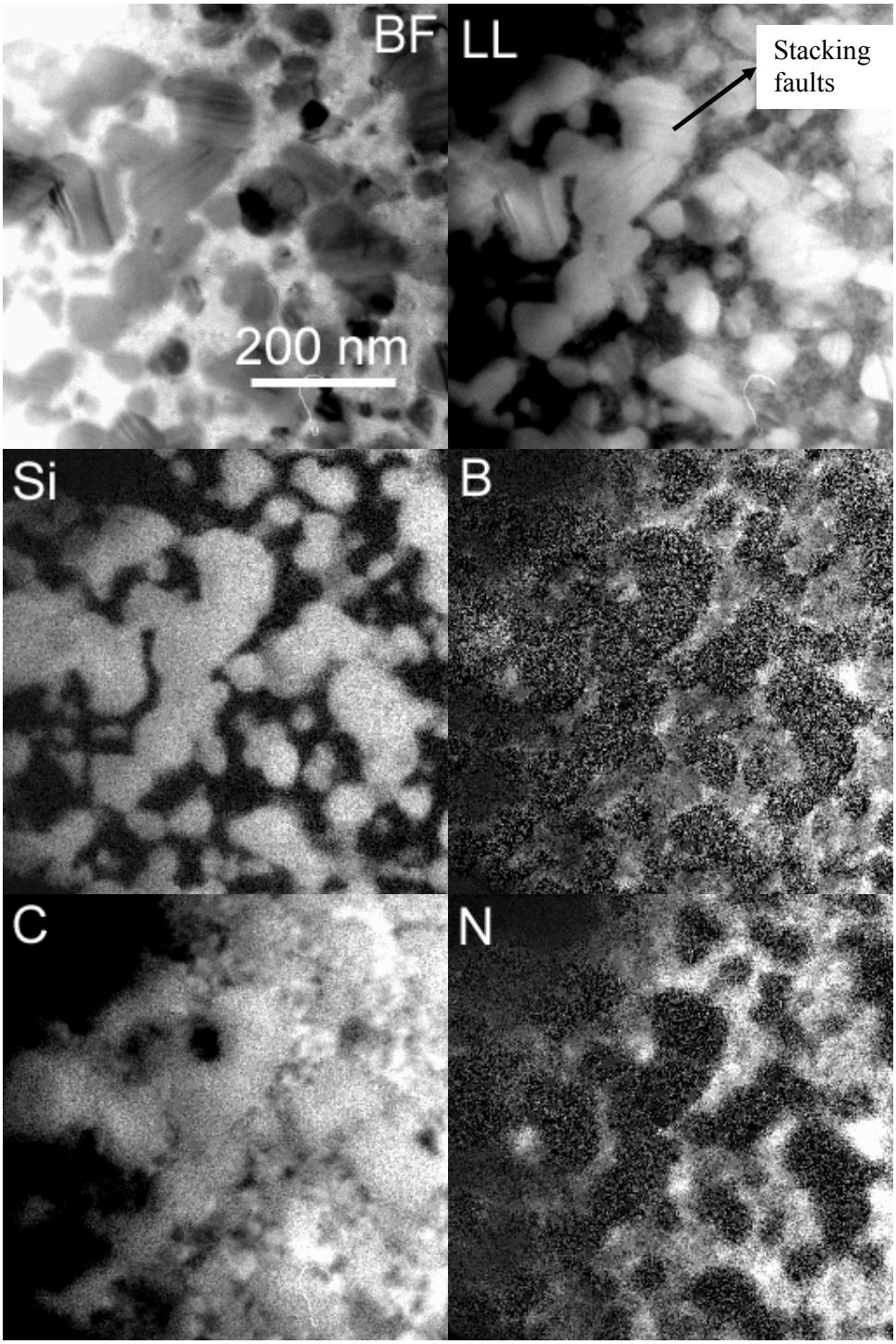

Figure: 4.3 (c) Bright field, low loss and elemental distribution images of Si-B-C-N ceramics crystallized at 1900 °C/3 h/1 MPa N_2 (32 - 80 μm).

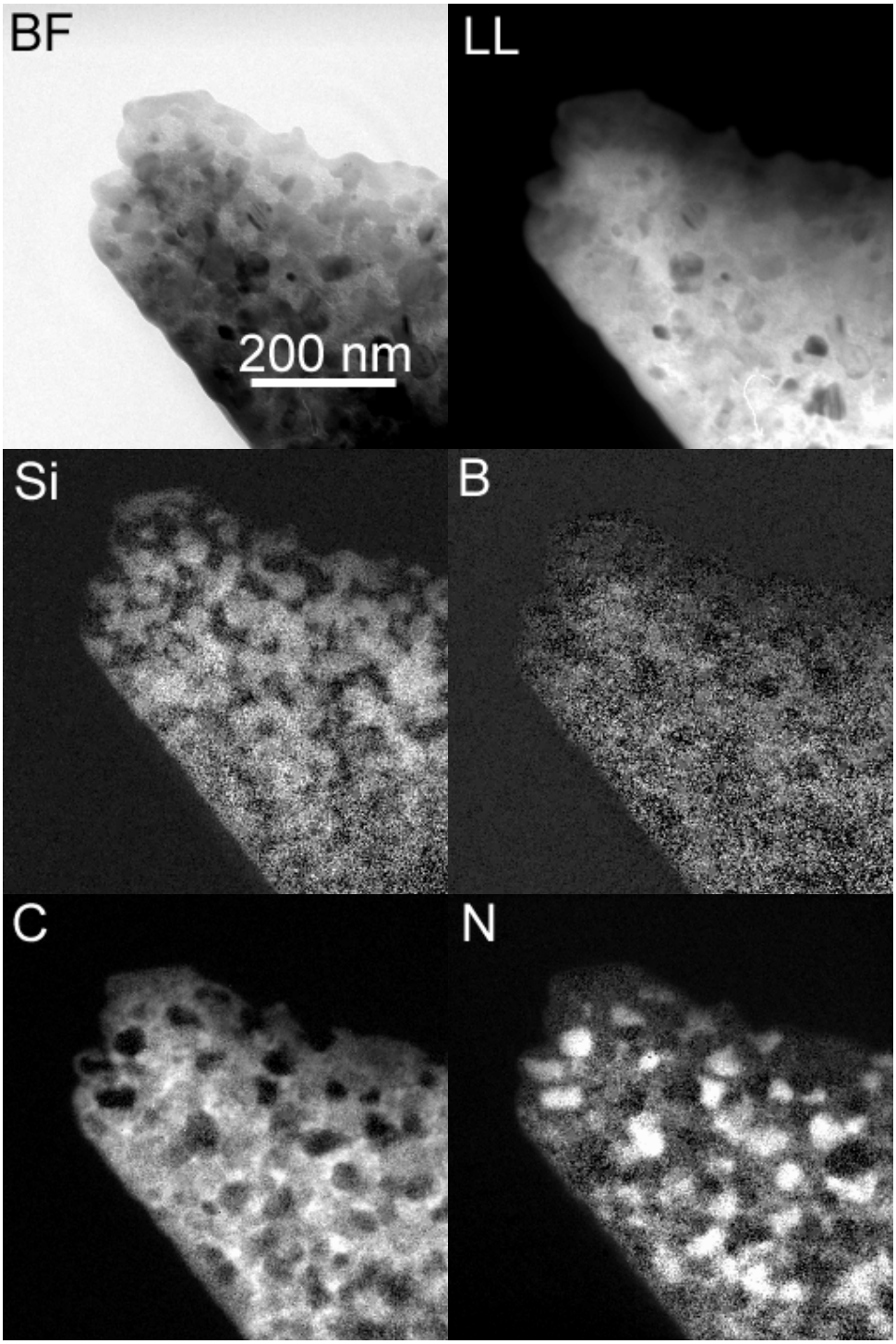

Figure: 4.3 (d) Bright field, low loss and elemental distribution images of Si-B-C-N ceramics crystallized at 1800 °C/10 h/1 MPa N_2 (80 – 160 μm).

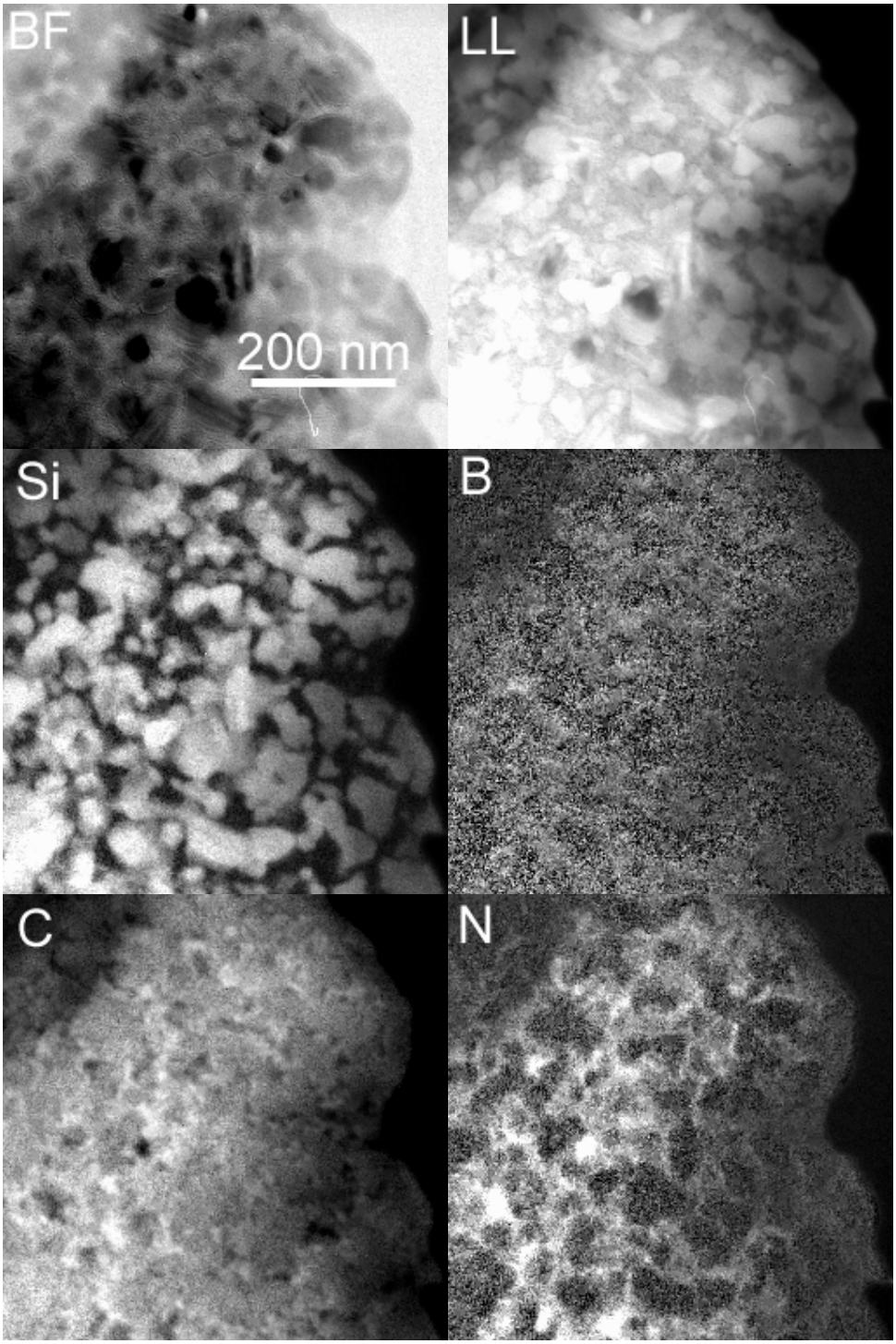

Figure: 4.3 (e) Bright field, low loss and elemental distribution images of Si-B-C-N ceramics crystallized at 1800 °C/10 h/1 MPa N_2 (32 - 80 μm).

Si-B-C-N ceramics annealed at 1800 °C for 3 h in a nitrogen atmosphere of 1 MPa show crystallites of SiC and Si_3N_4 in a matrix composed of boron, nitrogen and carbon (BNC phase). The crystallites were more or less spheroidal in morphology with an average size of

around 50 nm (Figure 4.3 (a)). Increasing the holding time at 1800 °C/1 MPa N_2 to 10 h results in a different nanostructure as shown in Figure 4.3 (d). The nitrogen map shows a significantly higher amount of nitrogen to be present in the material. Considering the Si, B, C and N maps collectively, one can confirm that there is a significant amount of Si_3N_4 in the material. Obviously, extending the holding time provided sufficient time for the Si_3N_4 to crystallize in the material. The extension of the holding time did not result neither in a drastic increase of the average crystallite size nor the grain shape.

On the contrary, annealing the material at the higher temperature of 1900 °C and holding it for 3 h in a nitrogen atmosphere of 1 MPa leads to grain growth to a size of about 50 nm - 100 nm (Figure 4.3 (b)). Most of the crystallites are seen to be SiC, while the presence of Si_3N_4 is minimal. Extensive crystallization of SiC leaves behind but a thin residual layer of the BNC matrix phase.

A pronounced influence of the size of the polymer particles used for processing on the crystallization behavior is also observed. Using polymer particles in the size range 32 μm - 80 μm (smaller size range), annealed at 1900 °C showed elongated crystallites (Figure 4.3 (c)). The crystallites are identified to be SiC while the elemental maps of Si, C and N, do not show any presence of Si_3N_4 crystals in the material. The SiC crystallites are as large as 200 nm or more, and seem to form an interconnected network distributed in the matrix. In contrast, for the same annealing conditions, the material produced using 80 μm – 160 μm polymer particles (Figure 4.3 (b)) contains at least some Si_3N_4 crystals.

4.1.4 Elastic Properties as a function of porosity/density

In the following, a nomenclature will be used which consists of a three digit number following the material's designation T21 which represents the warm pressing temperature (°C), i.e., 250 °C, 280 °C, 330 °C, used to consolidate the precursor powder to produce a

green body which essentially also controls the final density of the ceramic (refer Section 2.2.1).

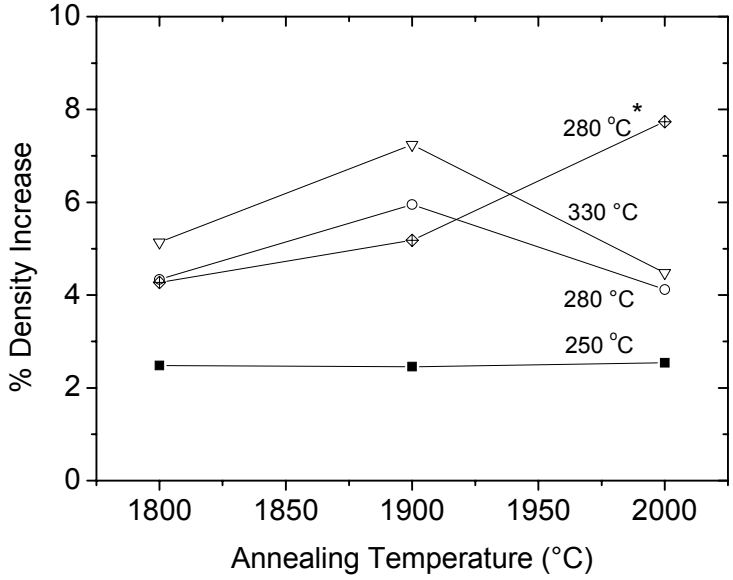

Figure: 4.4 Change in density of samples warm pressed at temperatures of 250, 280 and 330 °C as a function of the annealing temperature.

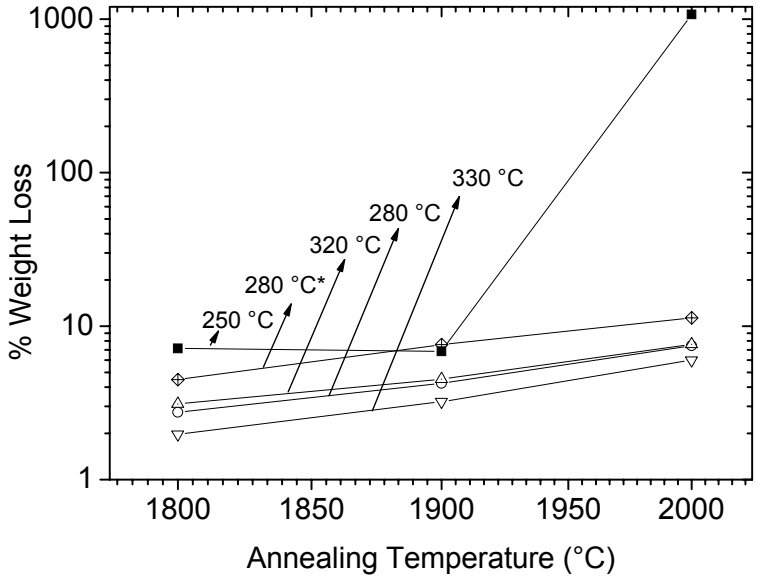

Figure: 4.5 Weight loss as a function of the annealing temperature of samples warm pressed at temperatures of 250, 280, 320, and 330 °C.

As seen from Table 2.3, the density increases as a result of higher warm pressing temperatures. In contrast, the density does not change much during annealing at temperatures

of 1800 °C to 2000 °C except may be for T21-280* (Figure 4.4). The weight loss of the samples was seen to follow a linear trend for all samples except T21-250 which exhibited an abnormal weight loss at 2000 °C (Figure 4.5).

Figure 4.6 shows ultrasonic transmission spectra of the samples which are extremal in terms of density, T21-250 and T21-330, both in amorphous and annealed conditions (although measurements were done for all the samples). At low frequencies the spectra oscillate in a complex fashion while at higher frequencies the magnitude decreases systematically. As observed in Figure 4.6, there is a clear difference in the magnitude spectra between the T21-250 and T21-330 samples. The spectra for T21-330 clearly show higher magnitude values in comparison to T21-250. A distinct difference in the magnitude spectra above 15 MHz can also be observed as a function of annealing temperature for T21-330, where, with increasing annealing temperature, the magnitude decreases as a function of frequency. For T21-330 the decrease in magnitude as a function of frequency is gradual, while for T21-250 there is a steep drop in the curves. For the T21-250 material annealed at 2000 °C, which had an anomalously high weight loss (Figure 4.5), the magnitude spectrum does not follow the usual pattern.

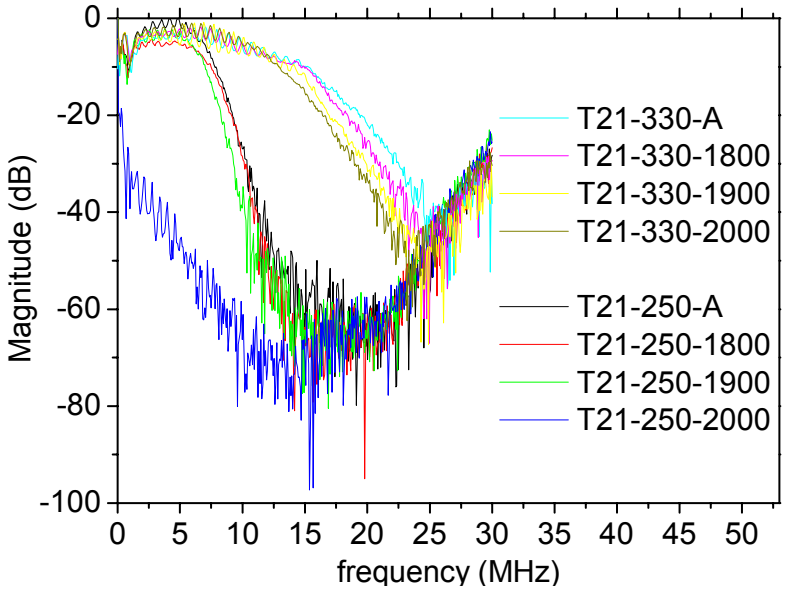

Figure: 4.6 Ultrasonic transmission spectra of T21-250 and T21-330 shown for comparison.

In Table 4.2, longitudinal and shear velocities of sound as extracted from the ultrasonic transmission spectra are tabulated for all samples along with the densities. For all samples a decrease in the longitudinal and shear velocities of sound is observed with increasing annealing temperatures, while the amorphous materials show the highest values. The elastic constant C_{ii} can be obtained from the sound velocity, due to

$$C_{ii} = \rho U^2 \cdot \quad (4.1)$$

Where i is the principal direction in which the measurement is performed, U is the longitudinal-wave velocity and ρ is the density of the material.

Sample name	Material condition	% wt loss after annealing	ρ_a g/cm^3	ρ_c g/cm^3	% increase in density	Longitudinal velocity m/s	E GPa	Shear velocity m/s	G GPa
T21-250-A	Amorphous	-	1.5521	-	-	4652.59	**34**	3088.29	**15**
T21-250-1800	1800 °C	7.17	1.6290	1.6694	2.48	4324.16	**31**	2927.67	**14**
T21-250-1900	1900 °C	6.86	1.5664	1.6050	2.46	3892.68	**24**	2552.82	**10**
T21-250-2000	2000 °C	10.72	1.6119	1.6530	2.54	4034.36	**27**	2652.16	**12**
T21-280-A	Amorphous	-	1.5947	-	-	5521.77	**49**	3815.16	**23**
T21-280-1800	1800 °C	2.75	1.6974	1.7711	4.34	5346.66	**50**	3546.50	**22**
T21-280-1900	1900 °C	4.24	1.6564	1.7550	5.95	4572.08	**37**	3192.34	**18**
T21-280-2000	2000 °C	7.45	1.6837	1.7530	4.12	4653.47	**38**	3246.80	**18**
T21-320-A	Amorphous	-	1.8159	-	-	6665.89	**81**	4810.32	**42**
T21-320-1800	1800 °C	3.12	1.8222	1.9541	7.24	6491.54	**82**	4235.47	**35**
T21-320-1900	1900 °C	4.51	1.8352	1.9495	6.23	5641.64	**62**	4070.89	**32**
T21-320-2000	2000 °C	7.61	1.8236	1.8690	2.49	5292.40	**52**	3782.70	**27**
T21-330-A	Amorphous	-	1.8464	-	-	6929.00	**88**	4532.00	**37**
T21-330-1800	1800 °C	1.98	1.8425	1.9372	5.14	6208.00	**76**	4153.00	**34**
T21-330-1900	1900 °C	3.22	1.8744	2.0102	7.24	5723.00	**64**	3840.00	**29**
T21-330-2000	2000 °C	6.00	1.8720	1.9560	4.48	5485.00	**60**	3825.00	**29**
T21-280-A*	Amorphous	-	1.8703	-	-	6480.69	**79**	4461.11	**37**
T21-280-1800*	1800 °C	4.48	1.8586	1.9361	4.27	5866.67	**66**	4110.90	**33**
T21-280-1900*	1900 °C	7.58	1.8539	1.9500	5.18	6878.36	**92**	3953.15	**30**
T21-280-2000*	2000 °C	11.35	1.8219	1.9630	7.74	5129.45	**52**	3664.19	**26**

Table: 4.2 Recorded values of longitudinal and shear velocities of amorphous and nano-crystalline Si-B-C-N ceramics as a function of annealing temperature and density using ultrasonic phase spectroscopy and the elastic moduli derived from these measurements. E = Young's modulus, G = shear modulus, ρ_a = density of the material in the amorphous state, ρ_c = density of the material in the crystalline state.

4.1.5 High temperature deformation

For the high temperature deformation investigations of T2-1 derived nano-crystalline Si-B-C-N ceramics samples annealed for 3 h in 1 MPa N_2 at 1800 °C (T21-1800) and 1900 °C (T21-1900) were selected.

4.1.5.1 Shrinkage

Amorphous precursor derived ceramics exhibit considerable shrinkage during creep deformation due to structural changes in the amorphous state which are induced by the temperature treatment (Figure 4.7) [01Ald]. The shrinkage component of the total deformation was determined by carrying out the creep experiments in the temperature range of 1350 °C, 1400 °C, 1500 °C at a negligible load of 5 MPa, which is just required to hold the specimen in position. As suspected under the same conditions the shrinkage of the crystallized materials is negligible as also shown in Figure 4.7.

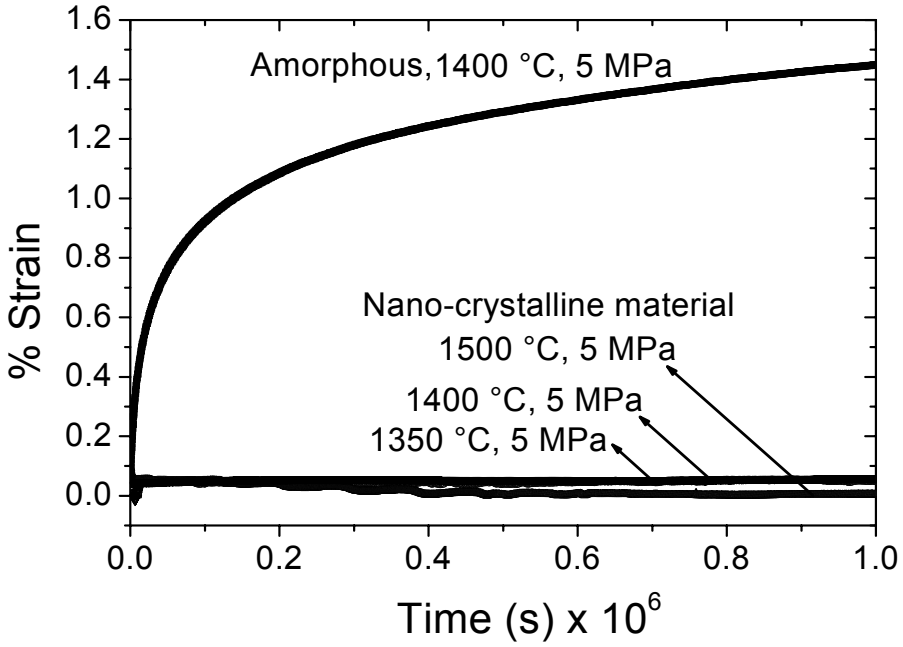

Figure: 4.7 Compression creep curves of amorphous and nano-crystalline Si-B-C-N ceramics (T21-1900) at different temperatures

The shrinkage of the nano-crystalline ceramics at 1350 °C – 1500 °C is less than 0.1 % as compared to 1.4 % exhibited by amorphous Si-B-C-N ceramics after 300 h.

4.1.5.2 Stress dependence of deformation

T21-1800: With increasing loading on this material for a duration of 100 h at 1400 °C the deformation increased to 1.3 % at 100 MPa (Figure 4.8 (a)). At 150 MPa the sample failed after a duration of 47.5 h and the strain to failure recorded was around 1.8 %. In Figure 4.8 (b) the deformation rate is plotted as a function of time is plotted for different loads. At all loads primary creep is observed upto $5 \cdot 10^4$ s. Above this time the strain rate becomes constant and increases again. A distinct dependence of the strain rate on the load is not been observed at 75 MPa, 100 MPa and 150 MPa, though a slight load dependence of the minimum creep rate was observed. The minimum creep rates achieved were around 3 x 10^{-10} s^{-1} at 5 MPa, 5 x 10^{-9} s^{-1} at 50 MPa, 1.1 x 10^{-8} s^{-1} at 75 MPa and 1.4 x 10^{-8} s^{-1} for 100 MPa and 150 MPa.

The deformation rates at 1500 °C are plotted as a function of time in Figure 4.9. As compared to the results at 1400 °C, at this temperature of 1500 °C the primary creep is not so load dependent at the beginning and the curves show a distinct dependence of the minimum strain rate on the applied load. As the creep rates approach a minimum, a distinct load dependence can be observed also at this temperature. The primary creep regime is also shortened with increasing load. None of the samples failed during 200 h of creep time in the load regime tested. The minimum strain rates achieved between 25 MPa – 100 MPa are 3.9 x 10^{-9} s^{-1} to 2.3 x 10^{-8} s^{-1}.

T21-1900: The load dependence of the deformation of this material at 1400 °C is shown in Figure 4.10. After 300 h, maximum deformation is around 1.6 % to 1.7 %. The deformation rate decreases as a function of time for all loads and no minimum followed by an increase of the strain rate is observed. At all three loads there is a tendency that the strain rate exhibits a

constant value for a small period of time and after that, continue to decrease. The detailed reasons for the well different behavior of the material derived from T2-1 and annealed at 1800 °C different to that annealed at 1900 °C and abnormal to that of materials derived from MW-33 (Chapter 3) are not clear. However, this may be due to the fact that the materials obtained from T2-1 oxidized during creep testing, which will be discussed in detail, later in this chapter.

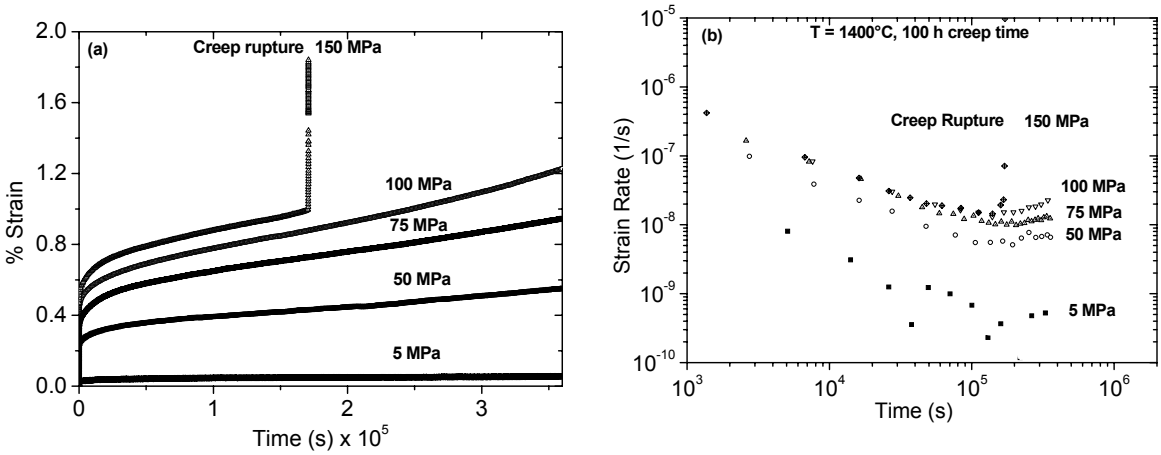

Figure: 4.8 (a) Deformation as a function of time for various loads at a temperature of 1400 °C recorded for material T21-1800. (b) Creep rates as a function of time in the load regime of 5 – 150 MPa during a creep time of 100 h.

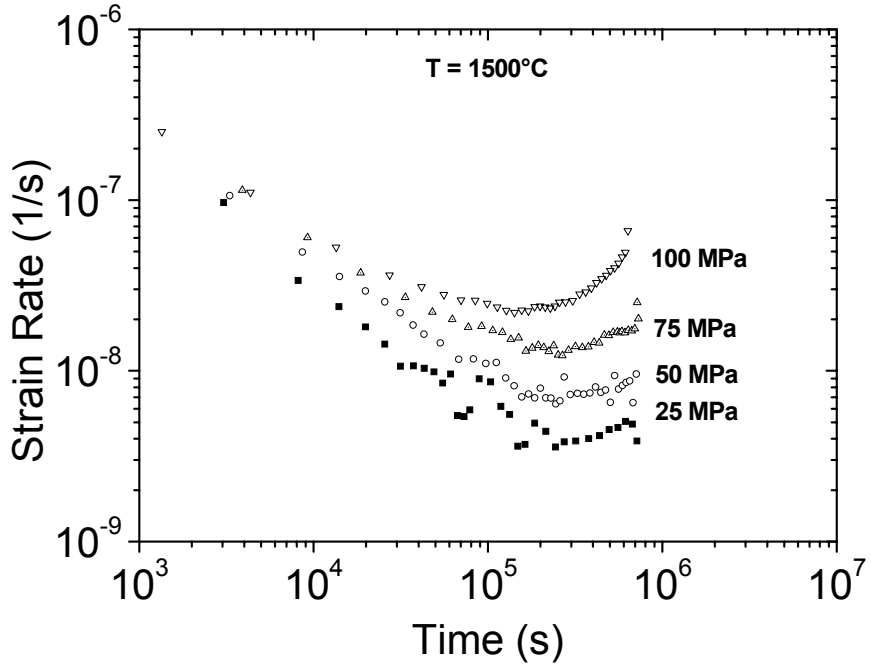

Figure: 4.9 Deformation rate as a function of time for various loads at a temperature of 1500 °C during a creep time of 200 h for T21-1800.

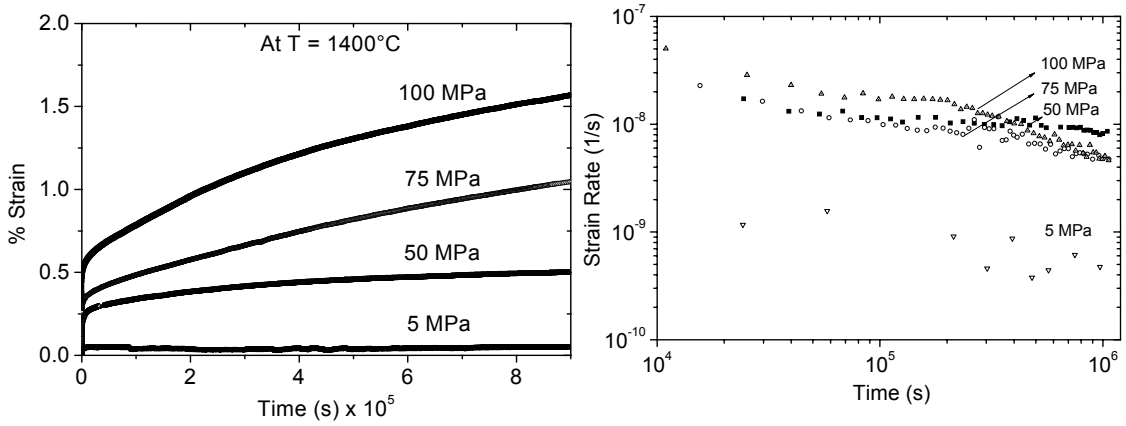

Figure: 4.10 Deformation and deformation rates of nano-crystalline Si-B-C-N ceramics as a function of time for various loads at a test temperature of 1400 °C for T21-1900.

4.1.5.3 Temperature dependence of deformation

T21-1800: A strong temperature dependence of the deformation and henceforth also of the deformation rate is observed for T21-1800. The deformation of the material at the lowest creep temperature tested (1350 °C) is ~ 0.3 % and at the highest temperature (1500 °C), the strain recorded is ~ 1.5 % at the end of 100 h (Figure 4.11). The deformation rate as a function of time shows different behavior with increasing temperatures. This can be seen more clearly in Figure 4.12. At 1350 °C, there is a continuous decrease in the creep rate at all times indicating rising creep resistance. At 1400 °C, the deformation rate curve exhibits a long primary creep region, with an order of magnitude increase in the creep resistance in the time frame tested. At around 10^5 s, an asymptotic approach to a minimum is observed. With the increase in the test temperature to 1500 °C, the primary creep is shortened and the strain rates become constant between 1 x 10^5 – 2 x 10^5 s. Beyond 2 x 10^5 s, the creep rate increases again and the curve clearly shows an upward trend as discussed in connection with Figure 4.9. Constant strain rates, with values of 5 x 10^{-9} s^{-1} and 2.4 x 10^{-8} s^{-1} are observed at temperatures

of 1400 °C and 1500 °C respectively. It is obvious that the strain rates reach a constant value for only a short time and increase with increasing temperatures.

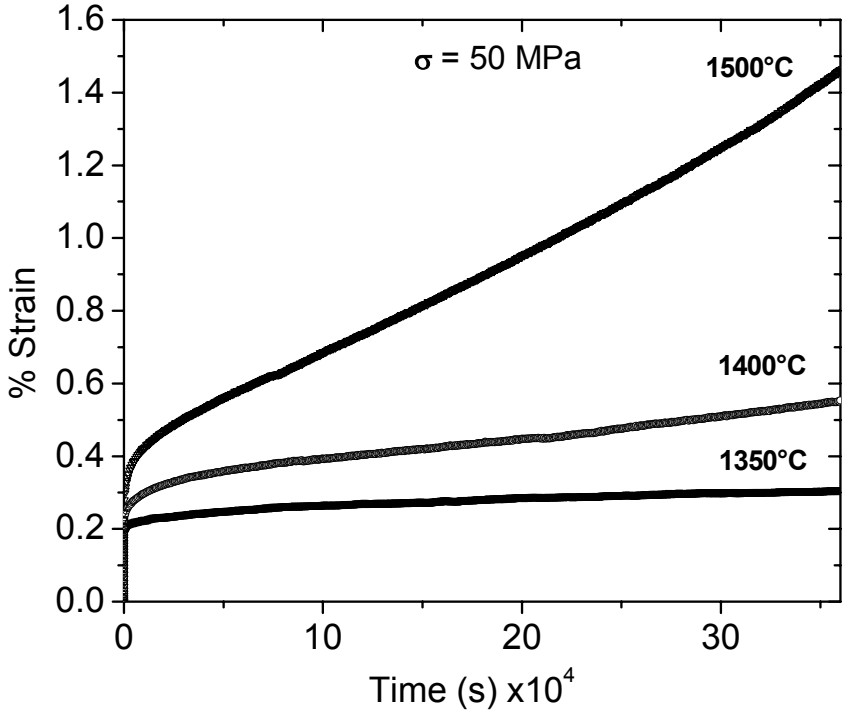

Figure: 4.11 Deformation as a function of time for various temperatures (1350 °C – 1500 °C) at a load of 50 MPa for 100 h for T21-1800.

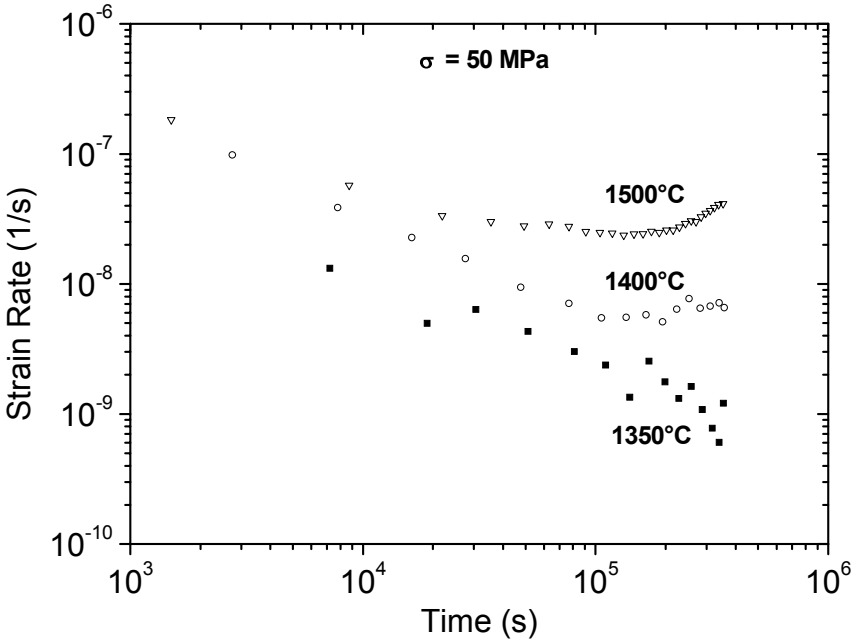

Figure: 4.12 Creep rates as a function of time in the temperature regime 1350 °C – 1500 °C carried out at 50 MPa load showing strong temperature dependence of the creep rates for T21-1800.

T21-1900: The deformation rate $\dot{\varepsilon}$ decreases continuously with time at all temperatures. Only at 1500 °C there is a tendency for an increasing strain rate beyond 6 x 10^5 s. It shows a strong temperature dependence throughout the creep tests and the curves run parallel to each other within the temperature range 1350 °C – 1500 °C upto 300 h of testing time as shown in Figure 4.13.

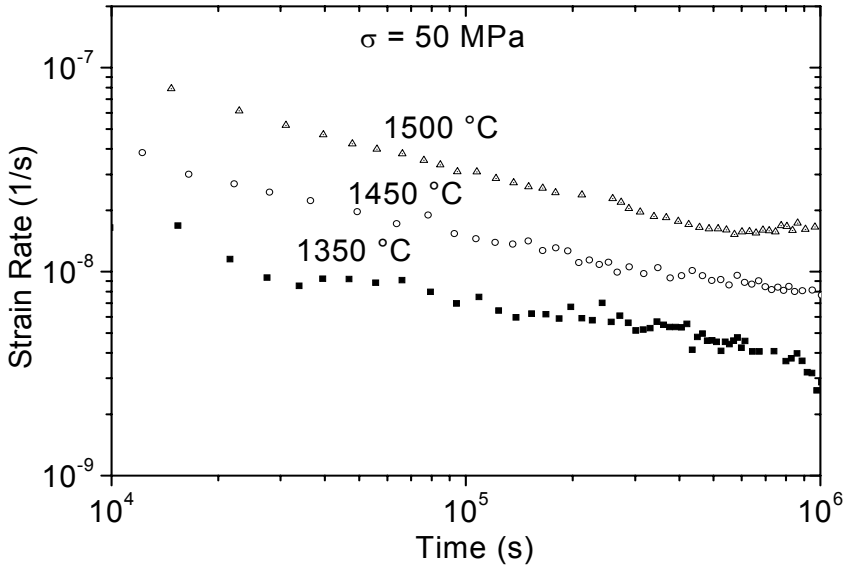

Figure: 4.13 Deformation rates of crystalline Si-B-C-N ceramics as a function of time at a compressive load of 50 MPa for various temperatures for T21-1900.

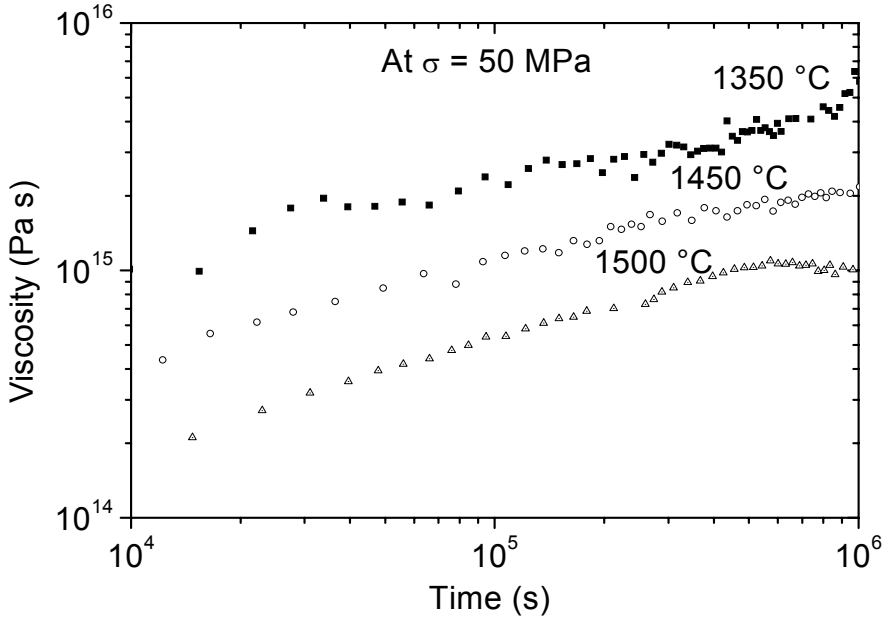

Figure: 4.14 Variation of viscosity as a function of time at a compressive stress of 50 MPa for various temperatures for T21-1900.

This is quite contrary to what is observed in the case of amorphous Si-B-C-N ceramics where the temperature dependence decreases with time and no temperature dependence is observed beyond 2 x 10^5 s [00Chr]. The viscosity was determined assuming Newtonian viscous flow using Equation 3.3 in the temperature range 1350 °C – 1500 °C at a constant load of 50 MPa. The viscosity values plotted as a function of time for various temperatures are shown in Figure 4.14. The viscosity increases linearly with time, and decreases with increasing temperature. Again, in contrast to amorphous Si-B-C-N ceramics, nano-crystalline ceramics show a strong dependence of viscosity on temperature at all times.

4.2 Discussion

4.2.1 Structural characterization

Since the crystallization processes that takes place in the closely related ceramics based on the polymer MW-33 is discussed in depth in Chapter 3, the discussion here is made short in order to avoid unnecessary repetition. Crystallization processes of these materials have been studied earlier, and it was observed that annealing of amorphous Si-B-C-N ceramics at temperatures higher than 1800 °C leads to the formation of SiC and Si_3N_4 with a mean grain size of 50 nm [01Bil]. This crystallite size is much less than what is observed for boron-free materials under similar annealing conditions.

The particles' size of the polymer has been found to have an influence on the materials high temperature stability. As the particle size is reduced, the surface area to volume ratio is increased which favors the decomposition of Si_3N_4 with temperature being sufficient at around 1900 °C for the decomposition to start. The effect of the size of the polymer particles on the decomposition behavior was also studied by Narayanan *et al.* [02Nar] where similar observations were reported. Furthermore, it was shown in [02Nar], that the extent of silicon nitride crystallization and its relative stability also depend on the size of the polymer particles. It was reported that the larger surface area of fine grained powders enables vapor phase

reactions that contribute to the decomposition of the materials. For a particle size larger than 315 μm a decomposition temperature of more than 2000 °C was observed, whereas a powder with a particle size between 32 μm – 80 μm decompose under the same conditions at about 1700 °C, in agreement with the results obtained here.

A close observation of TEM bright field and low loss images indicates that the larger SiC crystallites identified by the Si and C elemental maps contain striped contrast features, which are caused by the stacking faults included due to the formation of SiC polytypes in the grains. This is in close agreement with an earlier observation by Bunjes *et al.* [04Bun]. Almost all the SiC crystals showed such striped contrast features and the stripes were always parallel to the longest axis of the 2-dimensional section of the grains.

4.2.2 Elastic modulus

4.2.2.1 Influence of density/porosity

Precursor derived ceramics belong to the category where the materials are not 100 % dense and the pores in them are non-spherical. A non-destructive technique, namely, ultrasonic phase spectroscopy, is used here to determine elastic properties by measuring the wave velocities of sound. The Young's modulus for the differently processed and annealed materials are plotted versus density in Figure 4.15 (a). There is a distinct increase with increase in density for all materials.

The slope of the straight line connecting the data points as shown in Figure 4.15 (a), yield a value ~ 4.2, which is a measure of the performance index of these materials. In Figure 4.15 (b) the Young's modulus values of precursor derived Si-B-C-N ceramics determined from ultrasonic phase spectroscopy are plotted in an Ashby's material chart [89Ash] together with those of other engineering materials allowing a qualitative comparison. Engineering ceramics occupy the topmost position owing to the fact that they exhibit high modulus values.

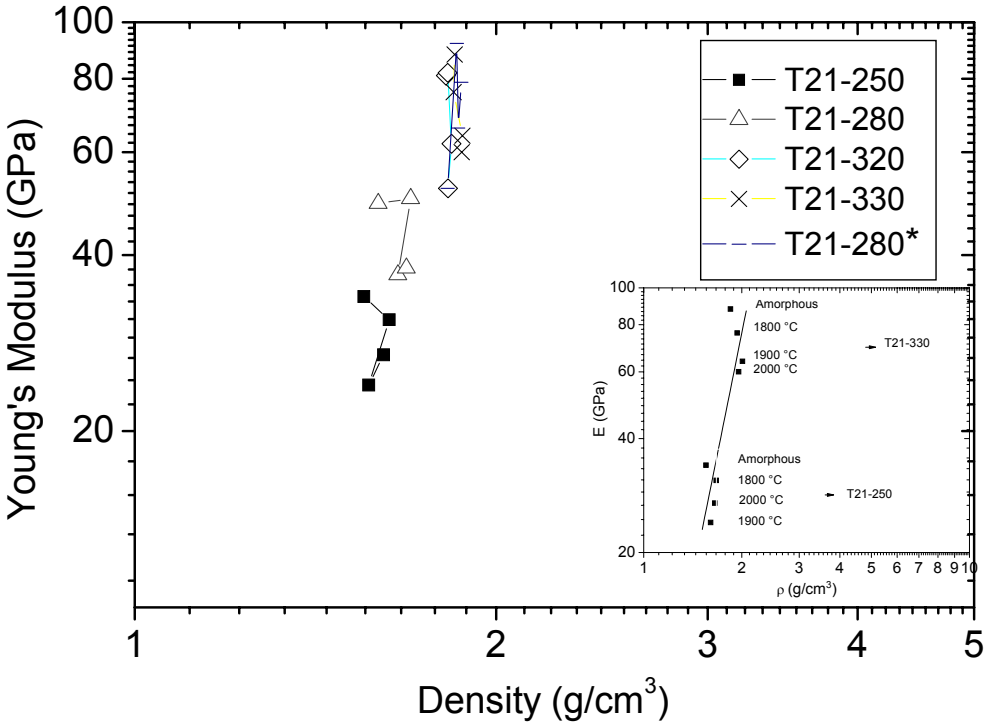

Figure: 4.15 (a) Young's modulus vs. density plot for all the materials under investigation. The groups of data points connected by lines correspond to different annealing treatments of the materials indicated, as detailed in Table 4.2

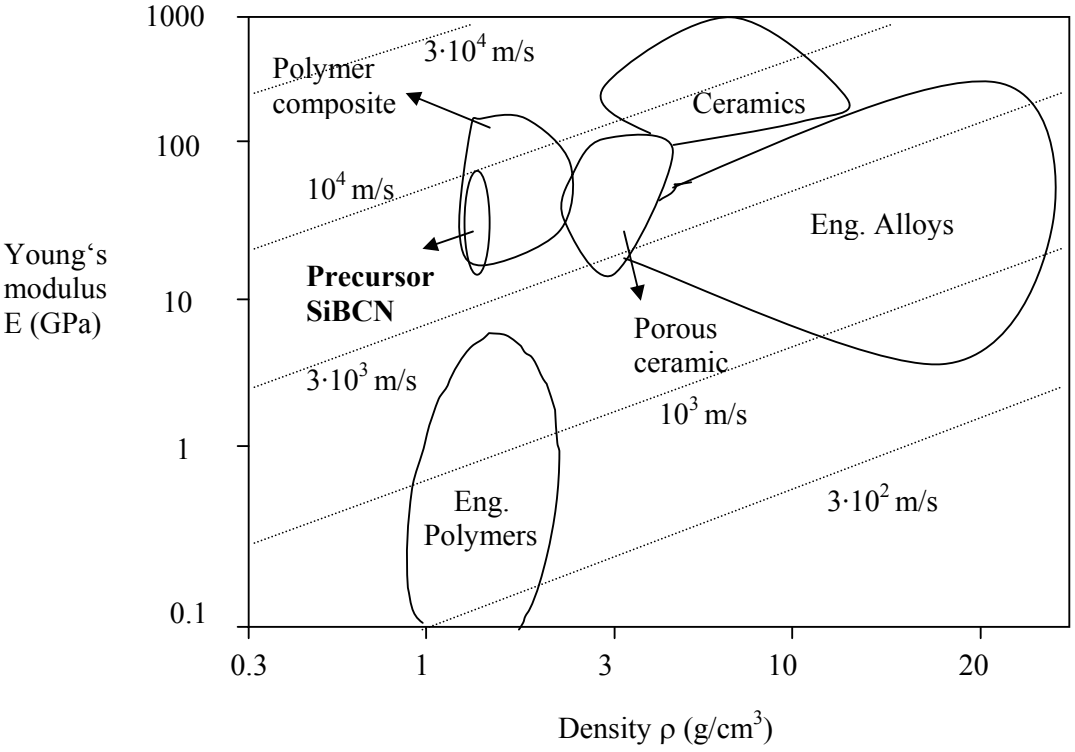

Figure: 4.15 (b) Modulus-density material property chart showing the results for Si-B-C-N ceramics in comparison with other materials.

Contrarily, porous ceramics are located at roughly half an order of magnitude lower sound velocities and at one order of magnitude lower moduli. However as can be seen from the chart, the E/ρ ratio for precursor derived Si-B-C-N ceramics is much higher than that of classical porous ceramics.

The slope of a straight line connecting the data point of a porous material with the corresponding zero-porosity material (100 % dense) can be regarded a measure of the efficiency with which the porosity reduces the effective modulus. The slope corresponds to the exponent η in the following equation:

$$\frac{E}{E_0} = \left(\frac{\rho}{\rho_0} \right)^{\eta} \tag{4.2}$$

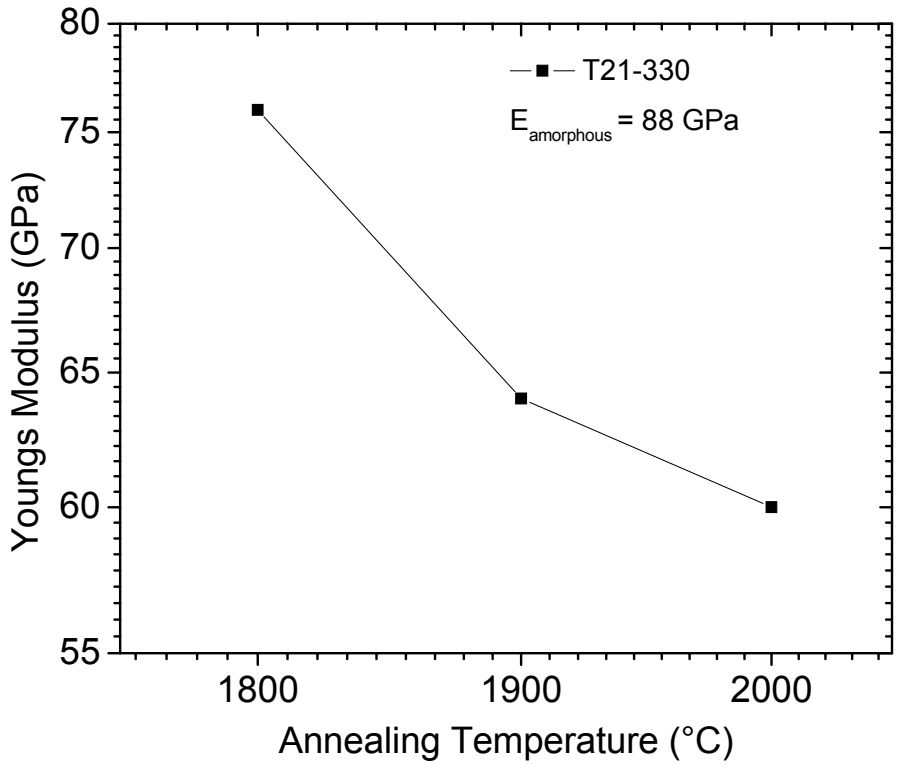

Figure: 4.16 Decrease in Youngs modulus values plotted as a function of annealing temperature for T21-330.

The exponent η is affected by the shape of the pores and by their orientation with respect to the loading axis or the wave propagation axis. A value of $\eta \sim 2$ holds for solids with randomly distributed spherical pores [90Ram] and for isotropic open cell foams [88Gib] over a wide range of relative densities. Wanner [98Wan] determined a value of 4.2 for a fibrous alumina material and a higher value of ~ 25 for plasma sprayed spinel. The high value seen for this material investigated by Wanner was attributed to the crack-like shape of the slit pores in the material. On the other hand, closed micro-cracks yield $\eta \sim \infty$ which means that the steeper the slope is, the higher is the possibility of existence of closed micro-cracks in the material.

As one can see from the Figure 4.15 (a) in connection with Table 4.2, there is a general trend for the elastic constants to decrease with increasing annealing temperature. As observed for example in the case of material T21-330 (Figure 4.16), the Young's modulus value decreases from 88 GPa amorphous state (T21-330-A) to 60 GPa after annealing at 2000 °C (T21-330-2000).

On the other hand, a systematic increase in the values of elastic modulus due to increasing density is clearly established from the values obtained for T21-250 to T21-330. Although increasing annealing temperature also causes an increase in density, this is over-compensated by some other effect. One plausible explanation could be that closed micro-cracks develop in the material as a result of the shrinkage which takes place during annealing. The internal strain and change in the phase composition (variations in the fractions of SiC and Si_3N_4) caused as a result of annealing may also affect the modulus values.

4.2.3 Deformation behavior

The high temperature deformation behavior of T2-1 derived ceramics differs substantially from that obtained from MW-33 polymer precursor. The most important difference is that the creep behavior consists of not only of a primary stage but also reveal stages of secondary and

tertiary creep (eg., Figures 4.8, 4.9 and 4.12). These results are not only inconsistent with the results obtained for the crystallized material discussed in Chapter 3, but also not in agreement with all other experimental results so far found with polymer derived materials either in their crystallized state [01Chr] or amorphous state [99Thu,00Chr,02Bau,02Zim]. While the MW-33 derived ceramics exhibited continuous decreasing strain rates even after 300 h of testing time during creep, T2-1 derived materials crystallized under identical conditions show a three stage creep behavior for all loads at 1400 °C and 1500 °C.

However, it should be emphasized that at the beginning, i.e., at 10^3 s the strain rates of both types of materials annealed at 1800 °C, and crept at 1400 °C are rather similar [T21-1800: 2 – 5 x 10^{-7} s^{-1} (50 – 150 MPa); MW-33 derived: 3 x 10^{-7} s^{-1} (100 MPa)] and the distinct difference develop only during creep with time and therefore may be due to the oxidation which takes place in T2-1 derived material. Microstructural investigations of the crept samples give insight in to the reasons for this anomalous behavior of T2-1 derived materials in comparison with the MW-33 derived materials.

4.2.3.1 Microstructural features

(i) T2-1 derived materials

T2-1 derived materials (both T21-1800 and T21-1900) exhibit large scale porosity as showed by microstructural investigations. From Figure 4.17 (a), it can be observed that the size of macro pores in the case of T21-1800 was as big as 200 μm, i.e., somewhat twice that of T21-1900 where in, the pore size was ≤ 100 μm (Figure 4.18 (a)). The microstructure of the crept T2-1 derived materials are obviously dominated by oxidation products formed during creep which may be due to the processing conditions used for their production. Figure 4.17 (a) and (b) show representative SEM images of T21-1800 in the secondary electron and backscattered mode before creep and after creep respectively.

However, the reason for the existence of such large macro-sized pores in T2-1 derived materials comes from the fact these materials were produced using larger sized polymer particles (80 μm – 160 μm) for compaction into a green body unlike the MW-33 derived materials. There are large voids created after the compaction, since these voids are unfilled due to the lack of smaller particles. The processing of these ceramics in this way results in the kind of porosity what has been observed for these materials as observed for T21-1800 (Figure 4.17 (a)) and T21-1900 (Figure 4.18 (a)). At higher annealing temperatures as in the case of T21-1900, the size of these pores however reduces further in comparison with T21-1800 though the morphology appears to be the same.

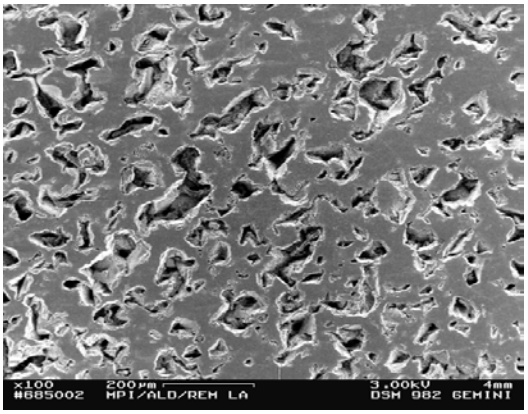

Figure: 4.17 (a) SEM micrograph of uncrept T21-1800 indicating the pore morphology, size and distribution.

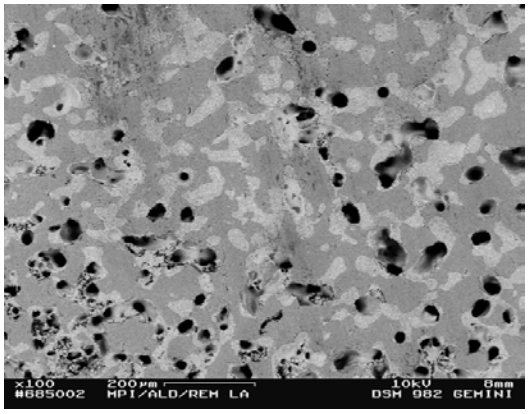

Figure: 4.17 (b) SEM micrograph of crept T21-1800 at 1500 °C/100 MPa after a duration of 200 h (refer Figure 4.9 for the corresponding strain rate curve).

The increasing amount of oxide formed during creep, as a function of time, in the pores of the material affects the measured creep deformation of the material. A quantitative comparison of the strain rates of T21-1800 with a MW-33 derived material crystallized under identical conditions and subjected to identical creep conditions (1400 °C/100 MPa) indicate that the strain rates of both the materials are similar in the beginning in the order of 2 – 3 x 10^{-7} s^{-1} at 10^3 s, and in the order of 10^{-8} s^{-1} at 10^4 s. At 10^5 s, T21-1800 does not show further decrease

in the strain rate contrary to its MW-33 counterpart which exhibits an order of magnitude decrease in the strain rate (10^{-9} s^{-1}) after the same duration of creep time (Figure 3.11 and Figure 4.8 (b)). Increasing strain rates observed in T21-1800 beyond 2 x 10^5 s (a deviation from the usual behavior of decreasing strain rate for long durations as in MW-33 derived materials) is a clear indication of the influence of oxidation on the time dependence of creep deformation at various loads (Figure 4.8 (b)).

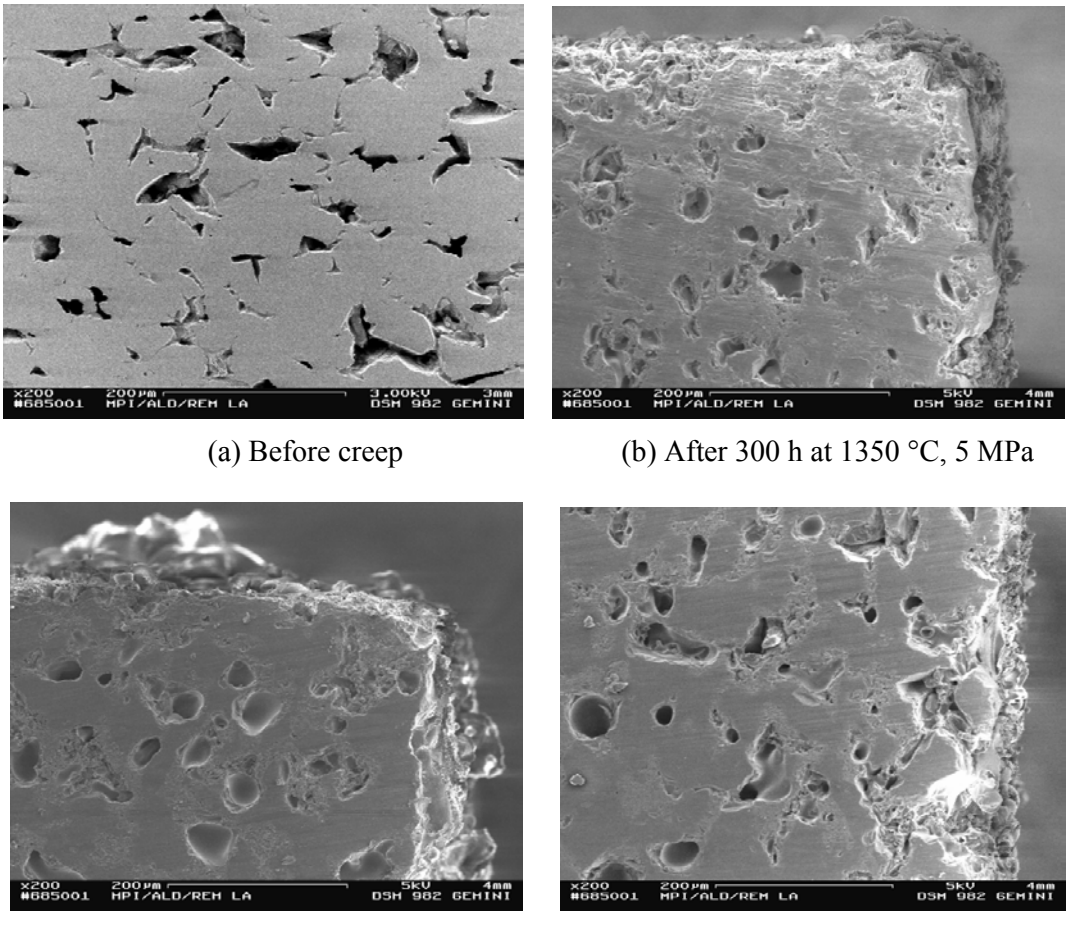

(a) Before creep (b) After 300 h at 1350 °C, 5 MPa

(c) After 300 h at 1400 °C, 5 MPa (d) After 300 h at 1500 °C, 5 MPa

Figure: 4.18 SEM micrographs of T21-1900 showing the morphology of porosity before and after creep. (b), (c) and (d) show the oxidation of the crept material at various temperatures.

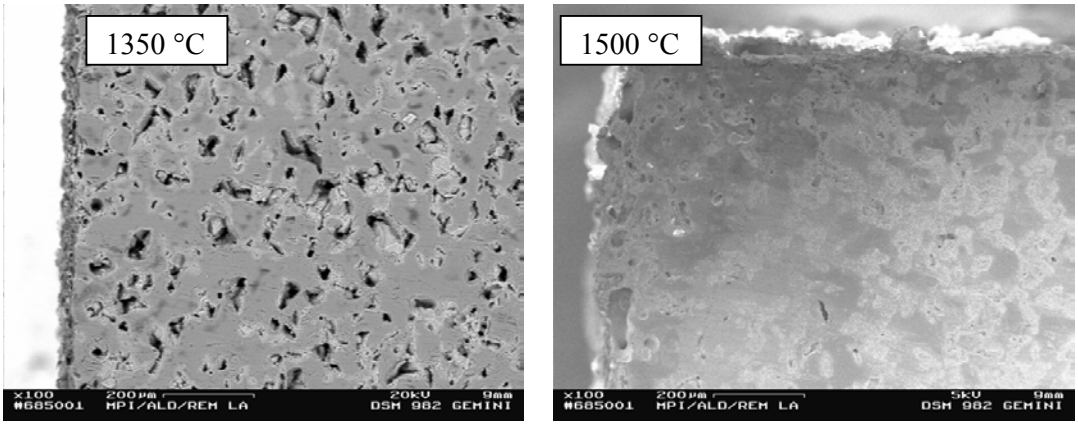

Figure: 4.19 SEM micrographs of crept samples of T21-1900 at 50 MPa after 300 h at 1350 °C and 1500 °C (refer Figure 4.13 for the corresponding creep curves).

The pore morphology of T21-1800 before seems to be more or less similar to that of T21-1900 excepting the pore size. There was an obvious change in the morphology of pores during creep, with some pores filled completely with oxide products and some partially filled as observed in Figure 4.17 (b). The pores are partially or completely filled depending of the creep temperature and time and hence can be said that the oxidation process is time and temperature dependent.

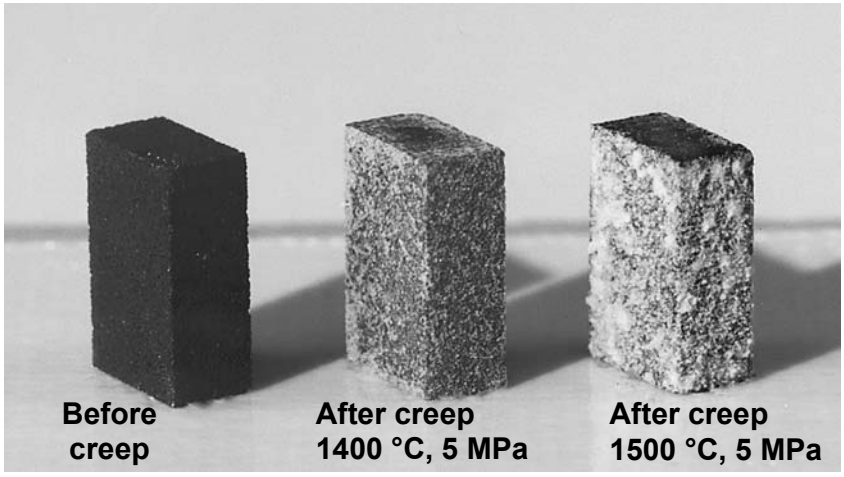

Figure: 4.20 Photographs of samples of T21-1900 subjected to high temperature oxidation for 300 h at 1400 °C and 1500 °C in comparison with a sample before the tests.

Extensive oxidation in T21-1900 was also observed as seen from the SEM investigations. The external oxidation of T21-1900 after creep testing at 1400 °C and 1500 °C in air is shown in

Figure 4.20. Obviously oxide surface layers are formed after 300 h. Their thickness was around 30 μm – 90 μm. As can be seen from Figures 4.18 to 4.22, substantial internal oxidation occurred during creep at 1350 °C to 1500 °C. The samples contain substantial amounts of fairly sized pores (Figure 4.18 (a)) whose inner surfaces will be coated at various temperatures with thick oxide layers (Figure 4.18 (b) to (d)) indicating that the pores are all open to the surface and the oxide formed at the sample surface cannot prevent internal oxidation. It was also observed that the pore morphology inside the specimen changed from a rather irregular shape in uncrept specimens to very rounded shapes in crept specimens (Figure 4.18).

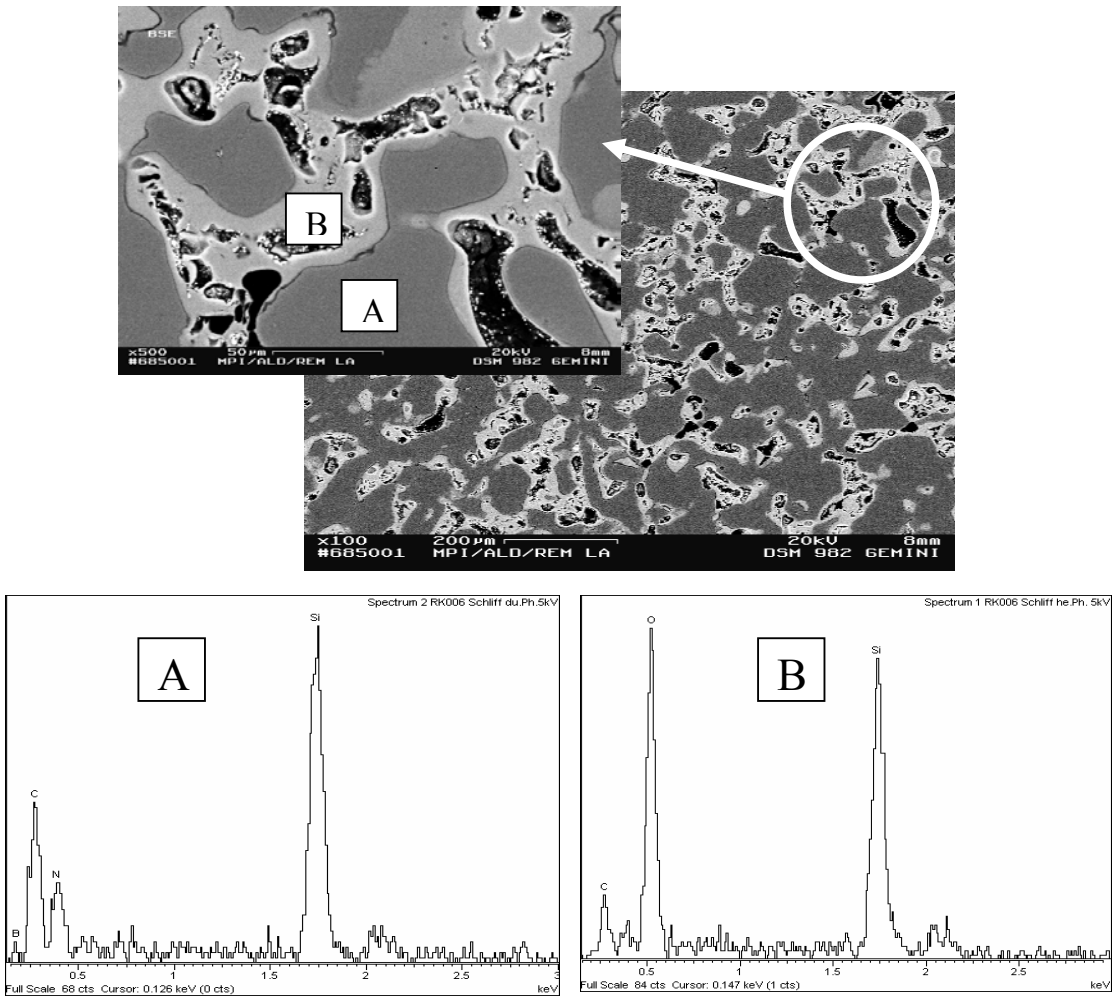

Figure: 4.21 Backscattered SEM images of crept samples of T21-1900 at 1350 °C, 5 MPa after 300 h showing incompletely filled pores with oxide scales. EDX shows the presence of oxygen in the brighter regions (B) and the absence in the darker regions of the material.

It was observed that while at 1350 °C the inner surface is coated with oxide as indicated in Figure 4.21, at 1500 °C the pores were filled with oxide products almost completely (Figure 4.22).

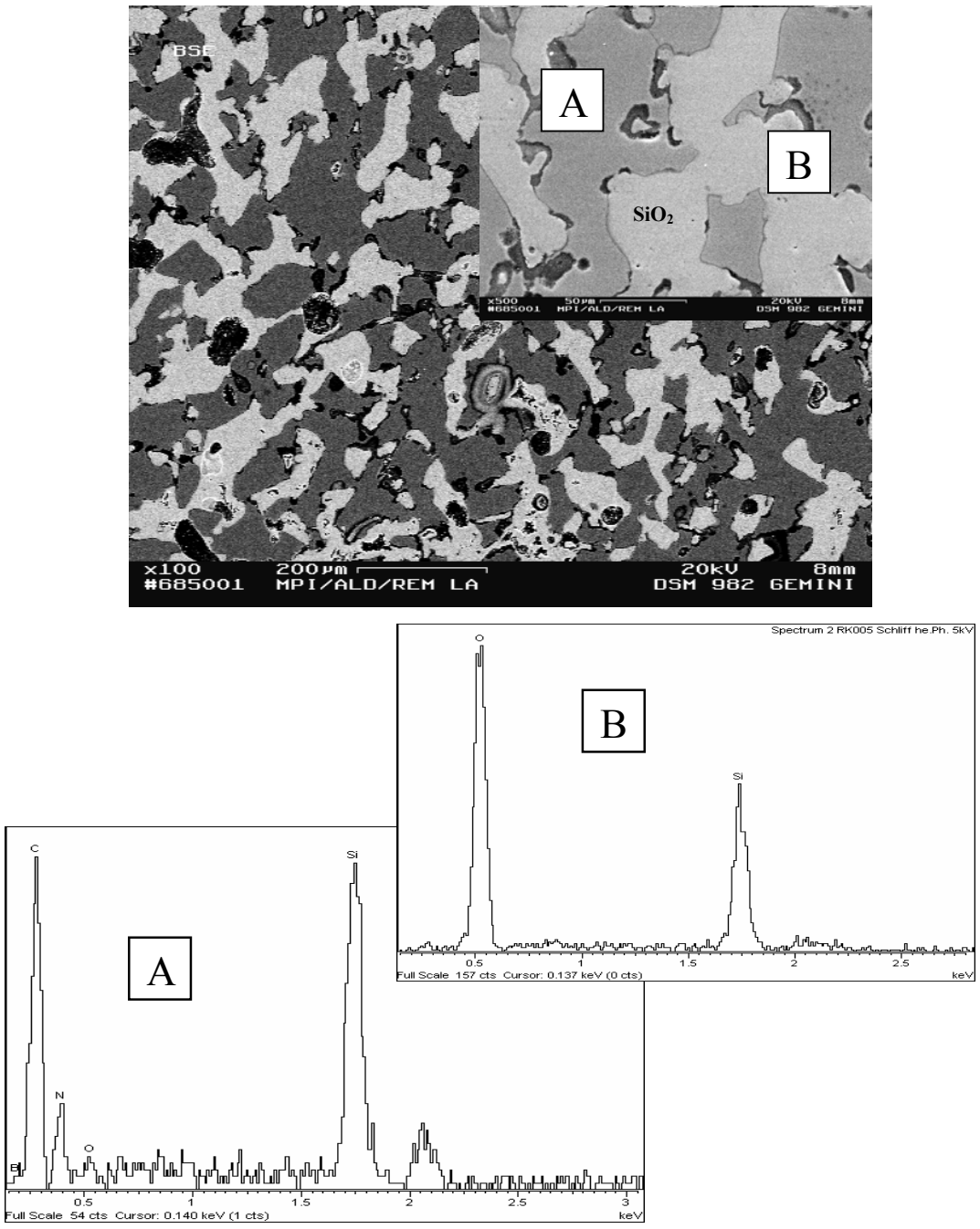

Figure: 4.22 SEM images in backscattering and secondary electron mode showing pores completely filled by oxide scales at 1500 °C, 5 MPa after 300 h in T21-1900. EDX measurements shows Si and O signals (B) in the brighter regions indicating the presence of SiO_2.

But the fact that T21-1800 in contrast to T21-1900, contained substantially higher amounts of large sized pores from the very beginning (prior to creep experiments) may explain the increasing strain rates of this material at longer times due to the increasing amount of low viscous oxide formed in the pores. This was true for all loads since after sometime of creep, the oxide phase becomes more dominant for the flow behavior and was more pronounced at higher testing temperatures since oxidation increased with temperature. Since the oxide-based glassy phase has a viscosity several orders of magnitude lower than those known from the amorphous Si-B-C-N based phases, the creep resistance of the material decreases severely and an increase of strain rate occurs with time which is quite normal for low viscous materials.

However, both the materials T21-1800 and T21-1900 investigated in the present work has a conglomeration of micro and nano pores associated with open pore channels. Figure 4.23 shows the same in the case of T21-1900. The extent of internal oxidation is governed by the size of the pore channels.

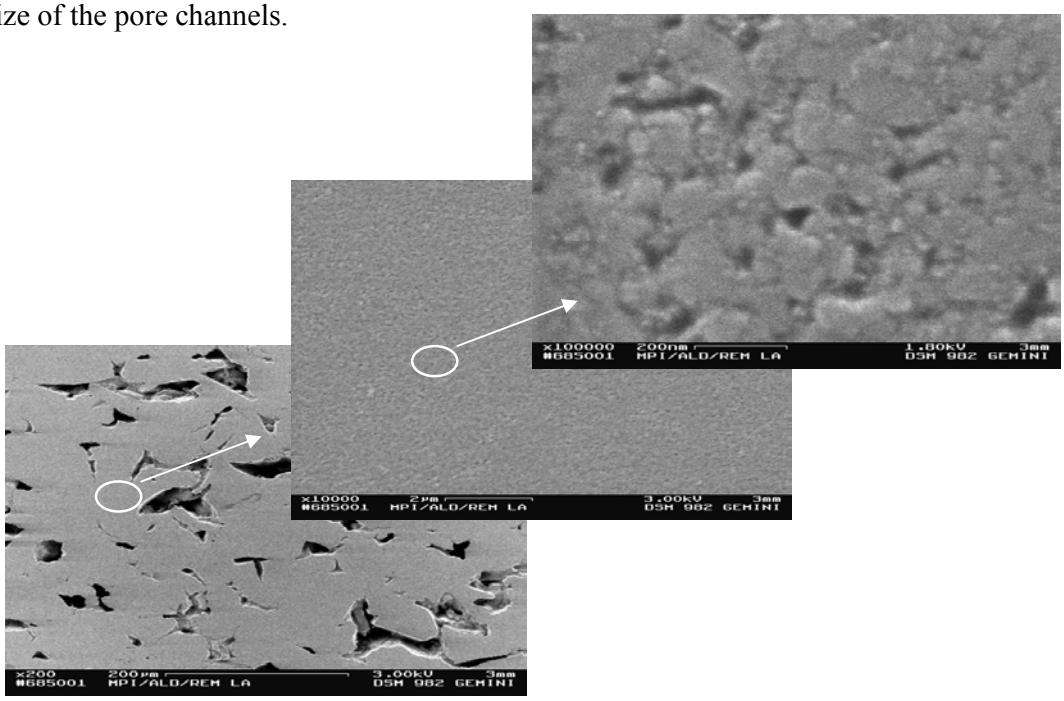

Figure: 4.23 SEM pictures showing micro (~ 50 µm) and interconnected nano-scale pores (30 – 40 nm) in T21-1900 annealed material. Elongated nano pores of the order of 200 nm with high aspect ratios were also seen in the material.

The oxidation occurs in two distinct stages as first described by Davidge *et al.* with reaction bonded silicon nitride [72Dav]. With time, the silicon oxide layer will be formed at the walls of the pore channels and more and more channels will be filled with oxide and thus the internal oxidation rate decreases to a lower level controlled by the diffusion of oxygen through the oxide formed (since SiO_2 has low permeability to oxygen) and in this stage in essence the oxidation is limited to the outer surface of the specimen. Several investigations of RBSN in the temperature range of 800 °C – 1500 °C have confirmed such a two stage oxidation process [84Por]. For the present materials, a similar two stage oxidation process can also be envisaged. A similar study on the oxidation kinetics of amorphous silicon carbonitride ceramics was also made envisaging a similar model [01Raj]. As a consequence of the closure of pore channels, i.e., the time of the beginning of the second stage of oxidation decreases with the diameter of the pore channels.

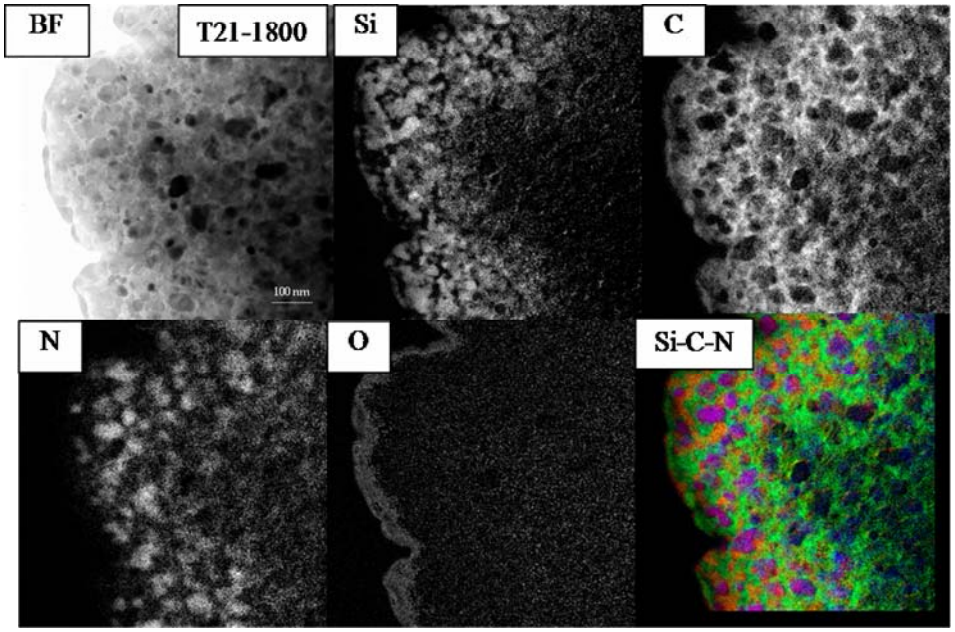

Figure: 4.24 (a) EFTEM of crept samples of T21-1800 tested at 1400 °C, 100 MPa. (Green = Matrix -BNC, Orange = SiC, Purple = Si_3N_4).

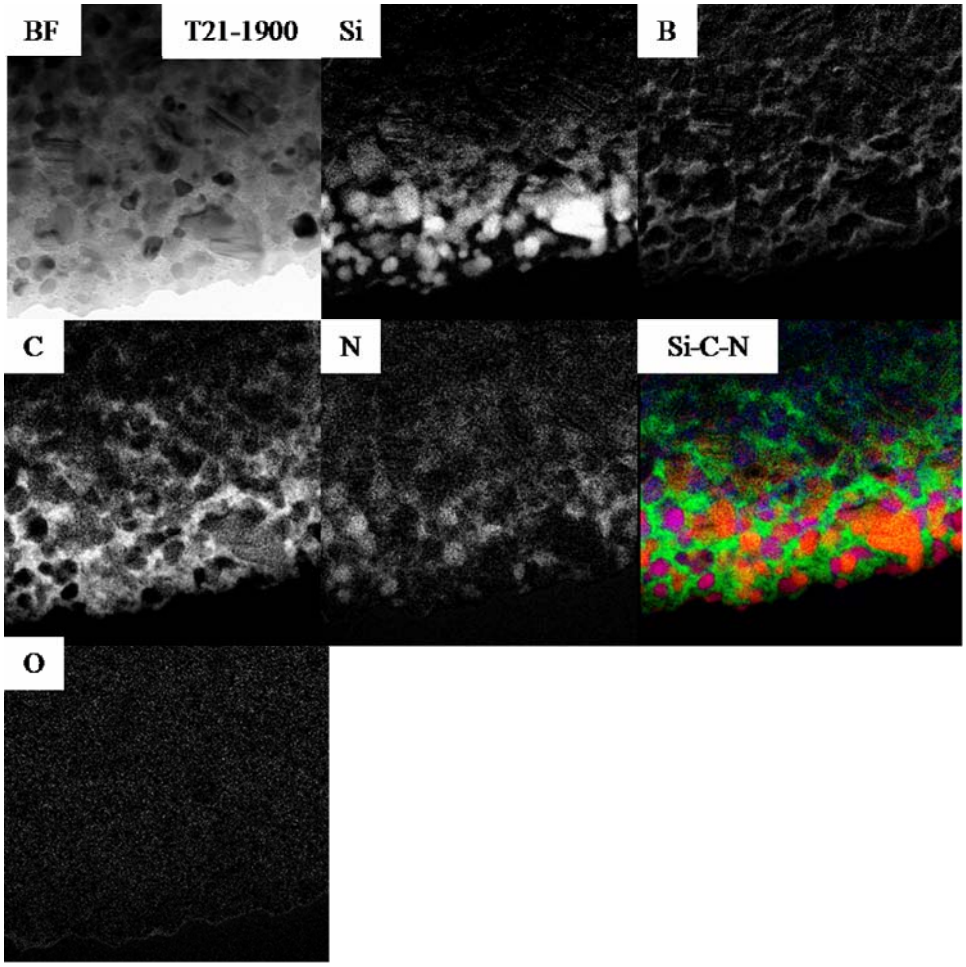

Figure: 4.24 (b) EFTEM of crept samples of T21-1900 tested at 1400 °C, 100 MPa. (Green = Matrix -BNC, Orange = SiC, Purple = Si_3N_4).

The EFTEM pictures of T21-1800 and T21-1900 tested under identical conditions (1400 °C/100 MPa) are shown in Figure 4.24. They provide information regarding the size and morphological details of the nano-crystallites in the material after creep. The figures also show chemical information obtained from three single elemental maps (silicon, carbon and nitrogen) coded in one color image.

The following observations can be extracted from the electron spectroscopic images.

- No difference in the morphology and size of the nano-crystallites before and after creep for both T21-1800 and T21-1900 is distinguishable, or at least it is difficult to

recognize such a change even if that happens at the level of a few nanometres (refer Figures 4.3 (a) and (b) for comparison).

- The oxygen map is completely dark in both cases, indicating absence of oxygen in the material. At least, the quantity must have been less than the detection limit. However this contradicts the information obtained from the SEM pictures of the crept samples where it was possible to observe extensive oxidation of the T2-1 materials (as discussed in Section 4.2.3.1).

Consequently, the EFTEM images of the crept samples could not explain the reason increasing strain rates in T21-1800 much earlier to T21-1900.

Subsequently, slow scan XRD spectra of T21-1800 and T21-1900 (Figure 4.25) show a drastic difference at low 2θ values. A broad peak (hump) observed for the material T21-1800 at 2θ = 10º to 25º is an indication of a substantial amount of residual amorphous phase still present in the material, in contrast to T21-1900 after annealing.

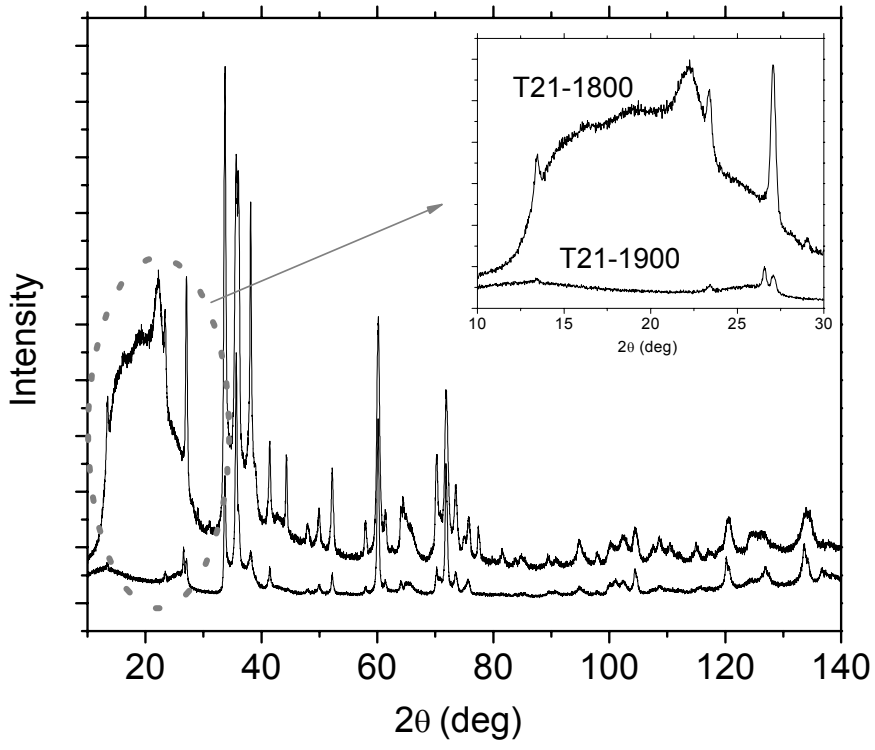

Figure: 4.25 Slow scan XRD spectra of T21-1800 and T21-1900 before creep showing a broad peak in the case of RK1800 between 2θ values of 10º - 25º.

However, the existence of an increased amount of amorphous phase still does not answer the observed increasing strain rates in T21-1800 in comparison with T21-1900. Hence, scanning electron microscopy of crept samples of T21-1800 and T21-1900 gives a better insight to the material state after creep which provides direct evidence in understanding the anomalous creep behavior observed in T2-1 derived materials.

To summarize it can be stated that the materials based on T2-1 polymer precursor investigated in this work were subjected to very strong oxidation during creep in air. As a consequence of that, the materials gradually lose its strong creep resistance typical of oxygen-free covalently bonded material to that of an oxide-based low-viscous glass after long durations. Nevertheless the results show that the creep resistance is substantially increased by the high temperature annealing of the as-thermolyzed materials. The beneficial effects of annealing these materials can be realized if the microstructure of these materials could be carefully controlled by producing denser compacts which in turn are possible by careful selection of the polymer particles. A brief discussion on the oxidation behavior of MW-33 derived materials during creep and high creep resistance associated with these materials as a result of limited internal oxidation is a direct evidence for the influence of oxidation on the creep behavior.

(ii) MW-33 derived materials

MW-33 derived ceramics exhibited oxidation characteristics different to that of the T2-1 derived material. The oxide scales were only around 40 μm – 50 μm thick and since its pore size was substantially smaller as observed from the scanning electron micrographs of crept samples (Figure 4.26) the open pores will close up in an early stage of oxidation and thus limiting internal oxidation.

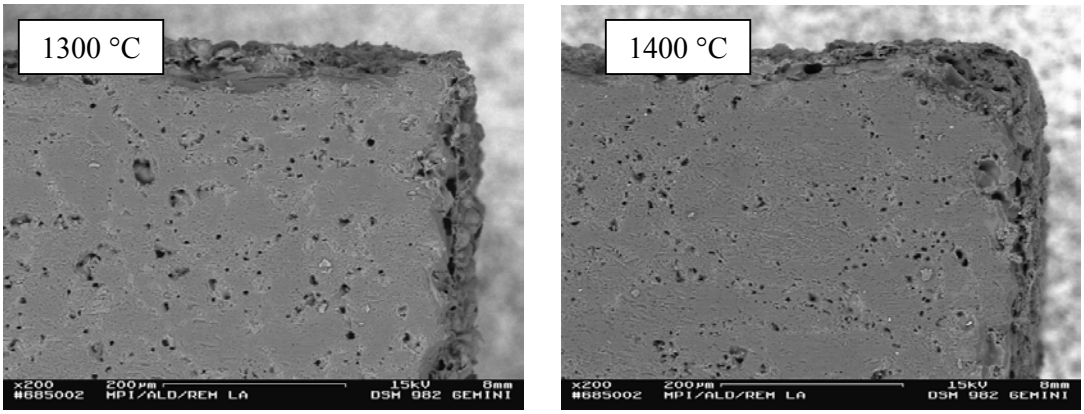

Figure: 4.26 SEM micrographs of crept samples of MW-33 derived samples (annealed at 1800 °C) after a load change experiment at 1300 °C and 1400 °C for 300 h (refer to Chapter 3 for the creep curves).

From the microstructural characterization of MW-33 derived materials (Section 3.1.2, Chapter 3), in the as-annealed (prior to creep) samples, it can be concluded that the initial pore size was in the order of 10 μm, which is an order of magnitude lesser than what was observed for T2-1 materials (T21-1800 and T21-1900). This may be due to the fact that the particle size distribution was more uniform, with a wide range of distribution as compared to T2-1 derived materials. Around 40 % of polymer particles in the size range of 32 – 80 μm, and 18 % in the size range < 32 μm which were used for compaction which filled the bigger voids created in between large polymer particles (Table 2.2). This resulted in denser compacts. Therefore, internal oxidation was of minor importance in these ceramics which indeed exhibited excellent creep resistance with continuous decreasing creep rates even after 300 h of testing time. This is indicative of the fact that Si-B-C-N skeleton was not destroyed by oxidation here (discussed in Chapter 3) contrary to that observed for T21-1800 and T21-1900 described above.